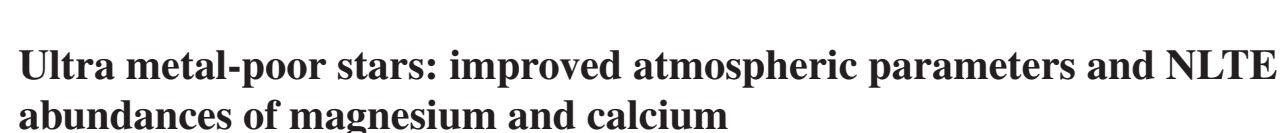
doi:10.1093/mnras/stz626





T. M. Sitnova, 1 to L. I. Mashonkina, 1,2 R. Ezzeddine 3,4 and A. Frebel 3,4

- ¹Institute of Astronomy, Russian Academy of Sciences, Pyatnitskaya 48, 119017, Moscow, Russia
- ²Department of Theoretical Physics, A. I. Herzen University, St Petersburg 191186, Russia
- ³ Joint Institute for Nuclear Astrophysics, Center for the Evolution of the Elements, East Lansing, MI 48824, USA

Accepted 2019 March 1. Received 2019 February 25; in original form 2018 December 29

ABSTRACT

The most metal-poor stars are the oldest objects, they provide a unique opportunity to study the earliest epoch of the Galaxy formation and individual nucleosynthesis events. These stars should be investigated with a scrupulous care, taking into account all available photometric, spectroscopic, and astrometric informations. We determined atmospheric parameters for 17 ultra metal-poor (UMP) stars, using an extensive method based on colour- $T_{\rm eff}$ calibrations, isochrones, Gaia DR2 trigonometric parallaxes, and non-local thermodynamic equilibrium (NLTE) analysis of the Ca I/Ca II ionization equilibrium and the Balmer line wings. We updated the model atom of Ca I- II by including recent quantum-mechanical rate coefficients for the Ca I + H I and Ca II + H I inelastic collisions. For any line of Ca I and Ca II in our sample stars, the changes in collisional data result in a shift of smaller than 0.05 dex in the NLTE abundance. We determined magnesium and calcium NLTE and LTE abundances of our sample stars. For 10 stars, we found close-to-solar [Ca/Mg] NLTE abundance ratios. In the remaining stars, magnesium and calcium abundances do not follow each other, such that [Ca/Mg] varies between -3.15 and +0.36, suggesting a contribution to stellar Mg and Ca abundances from a small number of supernova explosions with different properties. The obtained atmospheric parameters will be used in the forthcoming paper to determine NLTE abundances of chemical elements observed in spectra of the UMP stars.

Key words: atomic data-atomic processes-line: formation-stars: abundances-stars: atmospheres-stars: fundamental parameters.

1 INTRODUCTION

The atmospheres of low-mass stars contain information on the chemical composition of the interstellar medium at the time and place of their birth. Ultra metal-poor (UMP; -5 < [Fe/H] < -4) and hyper metal-poor (HMP; [Fe/H] < -5) stars (Beers & Cristlieb 2005) were presumably among the first stars, which were formed in the Galaxy after a small number of nucleosynthesis events. The determined abundance patterns of these stars can be matched to the yields calculated from supernova models in order to infer the properties of the first massive metal-free (Population III) stars and their explosion mechanism (see e.g. Limongi, Chieffi & Bonifacio 2003; Lai et al. 2008; Heger & Woosley 2010; Placco et al. 2016; Frebel et al. 2018). To determine accurate abundances, accurate atmospheric parameters are required. For example, an increase in $T_{\rm eff}$ from 5050 K to 5300 K results in 0.5 dex higher abundance

from the Mg Ib lines. Determination of atmospheric parameters of UMP stars is not a trivial task, and various methods possess their advantages and disadvantages.

One of the most common methods used to determine atmospheric parameters in wide range of spectral types and luminosity classes, including UMP stars, is a spectroscopic method based on determination of effective temperature ($T_{\rm eff}$) from the Fe1 excitation equilibrium, surface gravity (log g) from the Fe1/Fe1I ionization balance, and microturbulent velocity (ξ_1) from a requirement of the same abundance from lines of different strength. Thus, to determine $T_{\rm eff}$, log g, [Fe/H], and ξ_1 , only stellar spectrum is required, and this is considered as one of the main advantages of this method. The second advantage is that spectrum does not depend on interstellar (IS) reddening in contrast with photometric methods of $T_{\rm eff}$ determination.

However, in the atmospheres of metal-poor stars, the Fe I/Fe II number density ratio is subject to departures from the thermodynamic equilibrium value (Mashonkina et al. 2011; Bergemann et al. 2012; Amarsi et al. 2016; Ezzeddine, Frebel & Plez 2017; Lind et al.

⁴Department of Physics and Kavli Institute for Astrophysics and Space Research, Massachusetts Institute of Technology, Cambridge, MA 02139, USA

^{*} E-mail: sitnova@inasan.ru

2017). Therefore, the theoretical spectra have to be calculated based on the non-local thermodynamic equilibrium (NLTE) line formation for Fe I- II. Another shortage is that in spectra of UMP stars, the lines of Fe II are weak, if they can be detected at all. For example, among 20 stars with metallicity [Fe/H] < -4, the lines of Fe II in the visible spectrum range were detected only in six stars (Ezzeddine et al. 2017). In the near-UV range (2327-2343 Å), several Fe II lines exist that are stronger than all of those potentially available in the optical regime. However, observations in this spectral region are available for small number of UMP stars (Roederer et al. 2012, 2018; Ezzeddine & Frebel 2018). It is known that spectroscopic method gives systematically lower $T_{\rm eff}$ compared to those, derived from photometry. Frebel et al. (2013) found a difference between $T_{\rm eff}$ from Fe I lines and those, derived from photometric colours, of about 70-270 K depending on $T_{\rm eff}$ and suggested to use an empirical relation between these two temperature scales if accurate photometry is not available.

For UMP stars, calcium is the only element observed in two ionization stages and can be used for atmospheric parameter determination. Norris et al. (2007), Korn et al. (2009), Mashonkina, Korn & Przybilla (2007a), and Caffau et al. (2012) employed Ca I/Ca II ionization balance in NLTE to determine $\log g$ for UMP stars. It is worth noting that a detailed comparison of parameters derived from Ca I/Ca II and Fe I/Fe II for VMP stars is missing in the literature. The only comparison was presented for CD-38 245 ([Fe/H] = -4), where the NLTE abundance differences Fe I–Fe II and Ca I–Ca II do not exceed 0.11 dex in absolute value when photometric $T_{\rm eff}$ and distance-based $\log g$ are adopted (Sitnova, Mashonkina & Pakhomov 2018).

An application of hydrogen Balmer lines for $T_{\rm eff}$ determination requires accurate continuum normalization and line-formation calculations. For H α , NLTE leads to weaker line wings, which results in 80–100 K higher $T_{\rm eff}$ for VMP stars, compared to that derived in LTE (Mashonkina et al. 2010; Wu et al. 2015; Amarsi et al. 2018). The H γ line is less sensitive to NLTE effects and changes in log g compared to H α ; however, it is more sensitive to the convection treatment and it is more difficult to place continuum correctly due to lower signal-to-noise ratio (S/N) in the blue spectral region compared to those in the red. Deviations from LTE, 3D effects, and changes in $\log g$ do not affect significantly the wings of H β , and this line can serve as the most robust indicator of $T_{\rm eff}$ under classical 1D LTE spectral syntheses.

The spectroscopic methods strongly depend on model atmosphere and line formation modelling. When using photometric colours to determine $T_{\rm eff}$, interstellar reddening must be properly taken into account. The colour– $T_{\rm eff}$ calibrations are mostly tested with the [Fe/H] ≥ -3 stars (Alonso, Arribas & Martínez-Roger 1999; Ramírez & Meléndez 2005) due to poor statistics of the more metal-deficient stars with accurate infra-red flux method effective temperatures available. Therefore, using such calibrations for the UMP and HMP stars can lead to systematic errors in $T_{\rm eff}$.

Evolutionary tracks are widely used to determine $\log g$ for MP stars. However, this method does not allow to distinguish between a dwarf and a subgiant for G-stars. For giants, a small uncertainty in $T_{\rm eff}$ results in a large uncertainty in $\log g$.

For the first time, astrometric distances for a large number of UMP stars became available with Gaia DR2¹ (Gaia Collaboration et al. 2018) that makes possible to determine their log g. For comparison, at the time of Hipparcos (van Leeuwen 2007), trigonometric

parallax was measured for the only UMP star, G 77-61 ($\pi = 16.9$ mas). The first *Gaia* data release appended parallax measurement for one more UMP star, CD-38 245. However, for distant (d > 6 kpc) stars, errors of the *Gaia* DR2 parallaxes lead to uncomfortably large errors for log g, of more than 0.12 dex. The *Gaia* DR2 data suffer from a systematic shift in parallax (Arenou et al. 2018).

Taking into account the listed above advantages and disadvantages of different methods, we apply them for atmospheric parameter determination for the 17 most metal-poor stars known to date. Namely, we investigate lines of calcium in the two ionization stages and wings of the Balmer lines based on the NLTE line formation, use multiband photometry, isochrones, and *Gaia* DR2 parallaxes. As an initial guess, we use atmospheric parameters, derived by Ezzeddine et al. (2017) from spectroscopic method based on NLTE analyses of iron lines. We also determine magnesium LTE and NLTE abundance for the sample stars. In this study, we use [Mg/H] ratio instead of [Fe/H] as a main tracer of the chemical evolution, as it was recommended for MP stars by Fuhrmann (1998), Cayrel et al. (2004), and Andrievsky et al. (2010).

We outline the method of NLTE calculations for Mg I and Ca I—II in Section 2. Section 3 describes stellar sample and observations. The literature data on atmospheric parameters of the investigated stars are reviewed in Section 4. A procedure of stellar parameter determination is presented in Section 5. The derived [Ca/Mg] abundance ratios are presented in Section 6. Our recommendations and conclusions are given in Section 7.

2 METHOD OF CALCULATIONS

In this section, we describe the model atoms for magnesium and calcium statistical equilibrium calculations and the programs used for computing the level populations and spectral line profiles.

2.1 Mg I model atom

The Mg I model atom, atomic data and main NLTE mechanisms were described in detail by Mashonkina (2013). The model atom is based on that of Zhao, Butler & Gehren (1998); however, it was updated by Mashonkina (2013) by including fine structure levels of the Mg I 3p $^3P^{\circ}$ term, which is connected with the Mg Ib lines, and by accounting for H I impact excitations and charge transfer processes Mg I + H I \leftrightarrow Mg II + H $^-$ with the rate coefficients from detailed quantum mechanical calculations of Barklem et al. (2012). Photoionization is treated by employing accurate cross-sections from the Opacity Project (OP; see Seaton et al. 1994 for a general review), which are accessible in the TOPBASE² data base.

2.2 Ca I-II model atom

For calcium, we apply the NLTE method treated by Mashonkina, Korn & Przybilla (2007b) and modified by Mashonkina, Sitnova & Belyaev (2017) by accounting for H I impact excitation and deexcitation processes and charge transfer processes $CaI + HI \leftrightarrow CaII + H^-$ with the rate coefficients from quantum mechanical calculations of Mitrushchenkov et al. (2017). Photoionization is treated by employing accurate cross-sections from the OP. We refer to the cited papers for details of atomic data implemented in the CaI-II model atom.

¹https://gea.esac.esa.int/archive/

²http://cdsweb.u-strasbg.fr/topbase/topbase.html

Here, we consider for the first time an impact on NLTE abundances of the recent quantum-mechanical data for the CaII + HI collisions from Belyaev, Voronov & Gadéa (2018) instead of approximate Drawinian (Drawin 1968, 1969) rates with scaling coefficient, $S_H = 0.1$. For the CaI + HI collisions, we apply rate coefficients updated by Belyaev et al. (2017) instead of those from Mitrushchenkov et al. (2017).

We tested how the use of new accurate collisional data impacts on NLTE abundances from different lines of Ca I and Ca II in model atmosphere with $T_{\text{eff}} = 4900 \text{ K}$, $\log g = 2.0$, $\xi_1 = 1.9 \text{ km s}^{-1}$, and [Ca/H] = -3.7. As shown in the earlier NLTE studies (see Mashonkina et al. 2017, and references therein), the departures from LTE for Ca I are ruled by radiative bound-free transitions from the ground (4s² ¹S) and low-excitation (3d ³D, 4p ¹P°) levels. The overionization of Ca I results in weakened Ca I lines and positive NLTE abundance corrections ($\Delta_{NLTE} = log A_{NLTE} - log A_{LTE}$). A replacement of the Mitrushchenkov et al. (2017) data with that of Belyaev et al. (2017) for the CaI + HI collisions leads to smaller NLTE effects and smaller NLTE abundance corrections. The changes in Δ_{NLTE} are smaller than 0.02 dex for Ca₁ 4226, 4318, 4454, and 6122-62 Å and 0.05 dex for Ca I 5588 and 6439-62 Å. For comparison, Δ_{NLTE} amounts to 0.16–0.2 dex for different lines in a given model atmosphere. An exception is the Ca I 4226 Å resonance line, for which Δ_{NLTE} is close to 0 (see Section 5.4 for explanations).

Ca II is the majority species, and the departures from LTE are minor for the Ca II H and K resonance lines, with $\Delta_{NLTE} < 0.02$ dex when either Drawinian or quantum-mechanical rates are adopted for the Ca II + H I collisions. For the Ca II excited states, the deviations from LTE in their populations are ruled by radiative and collisional bound–bound transitions resulting in strengthened infrared (IR) triplet lines (8498, 8542, and 8662 Å, transition 3d $^2\mathrm{D} - 4\mathrm{p}\,^2\mathrm{P}^\circ$), but weakened 3706 and 3737 Å lines (transition 4p $^2\mathrm{P}^\circ - 5\mathrm{s}\,^2\mathrm{S}$). Using quantum mechanical rate coefficients leads to smaller deviations from LTE compared to those derived with the Drawinian rates (S_H = 0.1) and reduces the NLTE abundance corrections in absolute value, by 0.02–0.04 dex for different subordinate lines of Ca II. While, in a given model atmosphere, the NLTE abundance corrections amount to -0.6 dex and 0.1 dex for the Ca II IR triplet lines and 3706 Å, respectively.

2.3 Programs and model atmospheres

The coupled radiative transfer and SE equations were solved with a revised version of the DETAIL code (Butler & Giddings 1985). The update was presented by Mashonkina et al. (2011). The pre-calculated departure coefficients were then used by SYN-THV_NLTE code (Tsymbal 1996; Tsymbal, Ryabchikova & Sitnova 2018; Ryabchikova et al. 2016) to compute the synthetic spectra.

Throughout this study, the element abundance is determined from line profile fitting. The integration of the SYNTHV_NLTE code in the IDL BINMAG code by O. Kochukhov³ allows us to obtain the best fit to the observed line profiles with the NLTE effects taken into account.

We used classical plane-parallel model atmospheres interpolated for given $T_{\rm eff}$, log g, and [Fe/H] in the MARCS model grid (Gustafsson et al. 2008). The iron abundances for our sample stars were adopted from NLTE determinations by Ezzeddine et al. (2017).

Full list of the investigated lines is presented in Table 1 along with the transition information, gf-value, excitation energy of the lower level, and damping constants (log γ_{rad} , log γ_4 , log γ_6). The line list for synthetic spectrum calculation was extracted from the VALD data base (Kupka et al. 1999; Ryabchikova et al. 2015). For the Ca II resonance lines and the Ca II IR triplet lines, we take into account the isotopic components.

3 STELLAR SAMPLE AND OBSERVED SPECTRA

Our stellar sample contains 17 UMP stars, from dwarfs to giants, taken from Placco et al. (2015). Majority of them were studied in several papers. For each star, Ezzeddine et al. (2017) presented a list of papers, where a given star was investigated, together with atmospheric parameters determined from spectroscopic method based on NLTE analyses of iron lines.

The characteristics of the stellar spectra, which were used in this study, are summarized in Table 2. Observed spectra were retrieved from VLT/UVES⁴ and Keck/HIRES⁵ archives or private collections. New observations in the blue (3330–4960 Å) and red (4830–9410 Å) spectrum region have been obtained for HE1424–0241 with the MIKE spectrograph (Bernstein et al. 2003) on the *Magellan/Clay* Telescope at Las Campanas Observatory. The observing set-up of 0.7 arcsec slit was used that yielded a resolving power of $R \sim 35\,000$ and $R \sim 28\,000$ in the blue and red spectral ranges, respectively. For the other stars, details of the observations and the data reduction can be found in the original papers.

4 LITERATURE DATA ON ATMOSPHERIC PARAMETERS

To determine and compare element abundances of different stars, first, a homogeneous set of atmospheric parameters is required. We review available in the literature determinations of T_{eff} and $\log g$ for each star of our sample. Different studies adopted different methods based on photometry, isochrones, spectrum energy distribution, wings of the Balmer lines, lines of iron and calcium. Table 3 presents the minimal and maximal T_{eff} and $\log g$ available in the literature for each star of our sample. For half stars of the sample, a spread in $T_{\rm eff}$ is larger than 100 K. The two most investigated stars, CD-38 245 and CS22949-037, whose atmospheric parameters were determined in more than ten papers each, show a large and similar spread of 330 K in $T_{\rm eff}$. The largest difference of 500 K in $T_{\rm eff}$ is found for J0140+2344. The lowest effective temperatures originate from either Roederer et al. (2014) or Ezzeddine et al. (2017), where $T_{\rm eff}$ s were determined with Fe I excitation equilibrium method. One can note that independent of either LTE (Roederer et al. 2014) or NLTE (Ezzeddine et al. 2017), the temperatures based on Fe I are lower compared to those, derived from the other methods.

For FG-type stars, when $\log g$ is determined from isochrones, two values of $\log g$ correspond to a given $T_{\rm eff}$, and one cannot distinguish a dwarf from a subgiant. In this case, a spread of the literature data on $\log g$ for a given star can exceed an order of value. For example, for J0140+2344, Norris et al. (2013) recommended $T_{\rm eff}=5703$ K and $\log g=3.36$ or 4.68. For giants, a single value of $\log g$ corresponds to a given $T_{\rm eff}$. However, a small uncertainty in $T_{\rm eff}$ results in a large uncertainty in $\log g$. A difference of 1.15 and 1.68 dex between

³http://www.astro.uu.se/~oleg/download.html

⁴http://archive.eso.org/wdb/wdb/adp/phase3_main/form

⁵https://koa.ipac.caltech.edu/

Table 1. The list of MgI, CaI, and CaII lines with the adopted atomic data. For the CaII resonance and IR triplet lines, wavelengths and log $gf\epsilon$ are presented for different isotopic components together with their atomic masses (the second column).

λ	$E_{\rm exc}$	log gf	$\log \gamma_r$	$\log \gamma_4$ (rad s ⁻¹	$\log \gamma_6$
(Å)	(eV)		$(\mathrm{rad}\mathrm{s}^{-1})$	cm ³)	$(\mathrm{rad}\mathrm{s}^{-1}\mathrm{cm}^3)$
MgI					
3829.355	2.70	-0.227	0.000	-4.560	-7.291
3832.300	2.71	-0.353	0.000	- 4.560	- 7.291
3832.304	2.71	0.125	0.000	- 4.560 - 4.560	-7.291
3838.290	2.71	- 1.527	0.000	-4.560	- 7.291 - 7.291
	2.71				
3838.292		0.397	0.000	-4.560	- 7.291
3838.294	2.71	- 0.351	0.000	-4.560	- 7.291
4167.271	4.34	-0.745	8.710	0.000	0.000
4571.096	0.00	- 5.623	2.340	- 6.460	- 7.770
5167.322	2.70	-0.870	7.990	-5.470	-7.267
5172.684	2.71	-0.450	7.990	-5.430	-7.267
5183.604	2.71	-0.239	7.990	-5.430	-7.267
5528.405	4.34	-0.498	8.720	-4.630	-7.179
Caı					
4226.728	0.00	0.244	8.360	-6.031	-7.562
4283.010	1.88	-0.136	8.320	-5.840	-7.720
4318.652	1.89	-0.139	8.320	-5.760	-7.720
4454.779	1.89	0.258	8.017	-5.596	-7.162
5588.749	2.52	0.358	7.853	-6.072	-7.538
5857.451	2.93	0.240	8.477	-5.424	-7.316
6122.217	1.88	-0.316	7.860	-5.320	− 7.189
6162.173	1.89	-0.090	7.860	-5.320	- 7.189
6439.075	2.52	0.390	7.649	-6.072	- 7.569
CaII	2.02	0.000	7.0.7	0.072	7.005
3706.024	3.12	-0.402	8.630	-5.530	-7.610
3736.900	3.14	-0.104	8.640	- 5.530	- 7.610
3933:	0.00	-0.104	8.207	-5.730	-7.760
3933.655	48	-2.623	6.207	- 3.730	- 7.700
	46				
3933.657	44	- 4.293			
3933.659		- 1.576			
3933.660	43	- 2.765			
3933.661	42	-2.084			
3933.664	40	0.092	0.102	5.500	7.761
3968:	0.00		8.193	-5.730	-7.761
3968.460	48	- 2.928			
3968.462	46	-4.598			
3968.465	44	-1.881			
3968.466	43	-3.070			
3968.467	42	-2.389			
3968.469	40	-0.213			
8498:	1.69		8.207	-5.700	-7.675
8498.020	40	-1.429			
8498.077	42	-3.605			
8498.098	43	-4.286			
8498.129	44	-3.097			
8498.181	46	-5.814			
8498.233	48	-4.144			
8542:	1.69		8.207	-5.700	-7.675
8542.088	40	-0.476			
8542.143	42	-2.652			
8542.165	43	-3.333			
8542.198	44	-2.144			
8542.252	46	- 4.861			
8542.307	48	- 3.191			
8662:	1.69	2.171	8.193	-5.700	-7.675
8662.138	40	-0.736	0.175	2.700	7.075
8662.193	42	-0.730 -2.912			
0002.173	74	- 2.712			

Table 1 - continued

λ	$E_{\rm exc}$	log gf	$\log \gamma_r$	$\log \gamma_4$ (rad s ⁻¹	$\log \gamma_6$
(Å)	(eV)		$(\text{rad}\text{s}^{-1})$	cm ³)	$(\mathrm{rad}\mathrm{s}^{-1}\mathrm{cm}^3)$
8662.215	43	- 3.593			
8662.258	44	-2.404			
8662.302	46	-5.121			
8662.357	48	-3.451			

different $\log g$ determinations is found for giants CD-38 245 and CS22949–037, respectively. A giant and subgiant scenarios with $\log g = 2.65$ and 3.41 were adopted for HE0057–5959 by Norris et al. (2013) and Jacobson et al. (2015), respectively.

Differences in atmospheric parameters, derived for a given star in different papers, are larger than the claimed accuracy. To fix $T_{\rm eff}$ and $\log g$, advanced approaches are required.

5 DETERMINATION OF ATMOSPHERIC PARAMETERS

To derive a homogeneous set of atmospheric parameters ($T_{\rm eff}$ and $\log g$), we rely on photometry, isochrones, wings of the Balmer lines, Ca I/Ca II ionization equilibrium in NLTE, and *Gaia* DR2 parallaxes. We applied the following strategy of atmospheric parameter determination. For each sample star, we determine $T_{\rm eff}$ from photometric colours and Balmer lines and calculate log g using trigonometric parallaxes from Gaia DR2. Then we select a pair of $T_{\rm eff}$ and $\log g$ that provides a reasonable position on the isochrone and consistent within the error bars NLTE abundances from Ca I and Ca II. To fulfil our requirements, we allow T_{eff} and $\log g$ to be varied within 200 K and 0.2 dex, respectively. The details on the different methods of parameter determination and the derived results for the sample stars are presented in the following subsections. Due to insufficient number of spectral lines in the observed spectra of the sample stars, we compute microturbulent velocity (ξ_t) using the empirical relation from Mashonkina et al. (2017). This relation was deduced from NLTE analyses of Fe I and Ti I lines in a sample of VMP giants with well-determined atmospheric parameters. It provides an accuracy of $0.2 \,\mathrm{km}\,\mathrm{s}^{-1}$ for ξ_1 . Our final atmospheric parameters are presented in Table 3.

5.1 Photometry

The photometric magnitudes were taken from the SIMBAD⁶ (Wenger et al. 2000) and 2MASS⁷ (Skrutskie et al. 2006) data bases. For those stars, where V and I_C magnitudes are not available or of low accuracy, we used colour transformations between SDSS and Cousins magnitudes from Jordi, Grebel & Ammon (2006). Exceptions are HE2139–5432 and HE0057–5959, for which neither V nor gri magnitudes are available. We adopted a colour excess E(B-V) from the Schlegel, Finkbeiner & Davis (1998) map. For the sample stars, we calculated photometric $T_{\rm eff}$, using $V-I_CJK$ colours and calibrations from Ramírez & Meléndez (2005, hereafter RM05) and Alonso, Arribas & Martinez-Roger (1999, hereafter A99).

Fig. 1 shows a comparison of effective temperatures derived from different colours and calibrations for our sample stars. For our

⁶http://simbad.u-strasbg.fr/simbad/

⁷http://irsa.ipac.caltech.edu/frontpage/

Table 2. Characteristics of the observed spectra.

Star, instrument ID $R(10^3)$ S/N		S/N	λ (nm)	Reference		
CS22949-037, 1	34	20-60	319–900	Cohen et al. (2013), C66H, C02H; PI:Shuler, A226Hr		
CS30336-049, 2	39, 31		330-490, 490-940	Norris et al. (2013)		
HE0057-5959, 2	39, 31	91	330-490, 490-940	Norris et al. (2013)		
HE0107-5240, 3	40		329-452, 478-681	Christlieb et al. (2004), 268.D-5745(A), 074.D-0387(A)		
HE0107-5240, 3	66.32	30	665-1042	Bessell, Christlieb & Gustafsson (2004), 70.D-0009(A),		
				076.D-0165(A)		
HE0233-0343, 3	50, 52, 57	25, 45, 20	328-456, 472-683, 570-946	Hansen et al. (2014), 076.D-0546(A)		
HE0557-4840, 3	41, 42	30, 30	330-452, 473-684	Norris et al. (2007), 276.D-5041(A)		
HE0557-4840, 3	40.97, 42.31	30, 30	302-388, 565-946	Norris et al. (2012), 380.D-0040(A)		
HE1310-0536, 3	50, 35, 57	65, 20, 30	373-499, 472-683, 565-946	Hansen et al. (2014), 077.D-0035(A)		
HE1327-2326, 3	46, 70, 70	40-200	305-387, 478-680, 572-947	Frebel et al. (2006)		
HE1327-2326, 4	60		305-460, 355-525, 403-680	Aoki et al. (2006)		
HE1424-0241, 1	34	30	320-834	Cohen et al. (2007), C14H, C231Hb, C239Hr		
HE1424-0241, 2	35, 28	10	333-496, 483-941	this paper		
HE2139-5432, 2	37, 30	86, 86	330-490, 490-940	Norris et al. (2013)		
HE2239-5019, 3	18, 37	20, 40	328-456, 472-682	Hansen et al. (2014), 076.D-0546(A)		
J0140+2344, 1	48	51	372-460, 466-560, 566-654	Norris et al. (2013)		
J0313-6708, 2	35, 29	80	330-490, 490-940	Keller et al. (2014)		
J1313-0019, 2	35, 29	45, 55	330-490, 490-940	Frebel et al. (2015)		
J2209-0028, 3	39	17-48	376-500, 570-750, 767-947	Spite et al. (2013), 087.D-0123(A)		

Notes. 1 = Keck/HIRES, 2 = Magellan/MIKE, 3 = VLT/UVES, 4 = Subaru/HDS.

The proposal ID are indicated for the spectra, retrieved from the archives.

Table 3. Stellar atmospheric parameters.

Data from the literature:				This study:			
Star	min; max $T_{\rm eff}$ (K)	Ref.	min; max $\log g$	Ref.	$T_{\rm eff}$ (K)	$\log g$ (CGS)	
CD-38 245	4520; 4850	R14; R96, N01	0.65; 2.33	R14; HC13	4850	1.8	
CS22949-037	4630; 4960	R14; N13	0.95; 2.10	R14; M95	4900	1.9	
CS30336-049	4685; 4827	E17; L08	1.19; 1.51	N13; L08	4800	1.4	
HE0057-5959	5200; 5413	E17; J15	2.65; 3.41	N13; J15	5400	3.0	
HE0107-5240	5050; 5100	E17; C04, N13	2.20; 2.30	C04, N13; E17	5300	2.5	
HE0233-0343	6020; 6100	E17; HT14	3.4	HT14, E17	6300	4.2	
HE0557-4840	4800; 4900	E17; N07	2.20; 2.40	N07; E17	5100	2.2	
HE1310-0536	5000	E17; HT14	1.9	E17; HT14	4850	1.7	
HE1327-2326	6130; 6180	E17; F05, A06, K07	3.7	F05, A06, K07, E17	6180	3.7	
HE1424-0241	5140; 5260	E17; N13	2.50; 2.80	C07; E17	5200	2.5	
HE2139-5432	5270; 5416	E17; N13	3.04; 3.20	N13; E17	5400	3.0	
HE2239-5019	6000	HT14, E17	3.5	HT14, E17	6000	3.5	
10140+2344	5600; 6100	E17; A13	3.36; 4.68	N13	5900	4.6	
10313-6708	5125	K14	2.30	K14	5125	2.3	
11029-1729	5811	C11	4.00	C11	5800	4.7	
11313-0019	5100; 5380	E17; A15	2.60; 3.00	F15; A15	5400	3.0	
J2209-0028	6440	S13	4.0	S13	6300	4.5	

Notes. A06 – Aoki et al. (2006), A13 – Aoki et al. (2013), A15 – Allende Prieto et al. (2015), C04 – Christlieb et al. (2004), C07 – Cohen et al. (2007), C11 – Caffau et al. (2011), E17 – Ezzeddine et al. (2017), F05 – Frebel et al. (2005), F15 – Frebel et al. (2015), HC13 – Hansen et al. (2013), HT14 – Hansen et al. (2014), J15 – Jacobson et al. (2015), K14 – Keller et al. (2014), L08 – Lai et al. (2008), M95 – McWilliam et al. (1995), N01 – Norris, Ryan & Beers (2001), N07 – Norris et al. (2007), N13 – Norris et al. (2013), R96 – Ryan, Norris & Beers (1996), R14 – Roederer et al. (2014), S13 – Spite et al. (2013).

sample stars, calibrations of RM05 and A99 provide consistent $T_{\rm eff}$ for each of (V-K) and (V-I) colours, with average differences of $T(V-K)_{\rm RM05}-T(V-K)_{\rm A99}=11\pm30\,\rm K$ and $T(V-I)_{\rm RM05}-T(V-I)_{\rm A99}=65\pm101\,\rm K$. For the majority of the sample stars, A99 calibration provides lower $T_{\rm eff}$ from (V-I) compared to those from (V-K) and $T(V-K)-T(V-I)=150\pm140\,\rm K$ (when excluding an outlier, HE2239–5019). For RM05 calibration, we found $T(V-K)-T(V-I)=100\pm147\,\rm K$. The difference between temperatures from (V-I) and other colours exceeds 300 K in two faint sample stars, namely HE2239–5019 and J1313–0019, with V=15.85 and 16.64 mag, respectively. We

suspect, for these stars, the errors in the I and g, r, i magnitudes are larger than the claimed ones, of not exceeding 0.01 dex (Beers et al. 2007; Ahn et al. 2012). For all sample stars, $T_{\rm eff}$ from (V-K) and (V-J) in RM05 calibration agree well and the average difference amounts to $T(V-K)-T(V-J)=-25\pm70$ K.

Finally, we conclude that temperatures from (V-K) colour in A99 calibration and (V-K) and (V-J) colours in RM05 calibration to be the most reliable and provide unbiased with respect to each other effective temperatures with a small scatter. For the sample stars, the difference between $T_{\rm eff}$ derived from the former colours never exceeds 150 K.

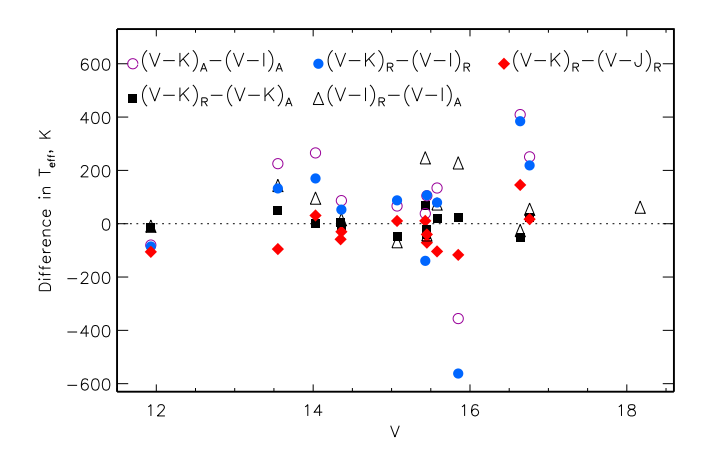


Figure 1. Difference between photometric temperatures derived from different colours and calibrations of Alonso, Arribas & Martínez-Roger (1999) and Ramírez & Meléndez (2005) as a function of the *V* magnitude for our sample stars.

It is worth noting that the colour- $T_{\rm eff}$ calibrations depend on metallicity, and they are supposed to be applied for stars with [Fe/H] > -2.5 and [Fe/H] > -3 in case of A99 and RM05 calibrations, respectively. The results presented in Fig. 1 were derived by adopting a similar metallicity [Fe/H] = -3 for all sample stars. Using [Fe/H] = -4 leads to 50 and 80 K higher $T_{\rm eff}$ from (V-K) for dwarfs and giants, respectively, and even larger differences for (V-I) and (V-J) colours, which depend on [Fe/H] stronger than (V-K). When individual [Fe/H] is adopted for each star, which ranges between -5.1 and -3.7, the difference between temperatures from different colours increases, for example, an offset between T(V-K) and T(V-J) in RM05 calibration becomes prominent and equals to -115 ± 82 K.

5.2 Balmer lines

In addition to photometry, we relied on the wings of $H\alpha$ and $H\beta$ to determine $T_{\rm eff}$. We adopted the NLTE method of H I line formation calculations from Mashonkina et al. (2008). The theoretical profiles of the Balmer lines were computed by convolving the profiles resulting from the thermal, natural, and Stark broadening (Vidal, Cooper & Smith 1970, 1973), as well as self-broadening (Barklem, Piskunov & O'Mara 2000). For the investigated range of atmospheric parameters, NLTE leads to weakened wings of $H\alpha$, which results in 80-100 K higher $T_{\rm eff}$, compared to those, derived in LTE. The NLTE effects increase towards higher $T_{\rm eff}$ and lower $\log g$. The wings of H α are sensitive to $T_{\rm eff}$ and $\log g$ variations. For example, $H\alpha$ line profiles calculated with atmospheric models 5900/4.6 and 5800/4.7 are similar. The wings of H β are better indicators of $T_{\rm eff}$, since they are much less sensitive to changes in $\log g$ and NLTE effects compared to H α . For four stars with different stellar parameters (a giant HE0107-5240, a subgiant J1313-0019, and dwarfs HE0233-0343 and J2209-0028), we show in Fig. 2 the effect of changes in T_{eff} and $\log g$ on the H α and H β line profiles. Depending on an S/N and continuum normalization of the observed spectra, we estimate an accuracy of $T_{\rm eff}$ determination from ${\rm H}\alpha$ and ${\rm H}\beta$ to be no less than 50 K and no more than 200 K. For faint stars with V of 16–18 mag and uncertain photometric $T_{\rm eff}$, we employed Balmer lines for $T_{\rm eff}$ determination. For the other stars, we checked that the adopted $T_{\rm eff}$ provides a reasonable fit to the wings of H α and H β in the observed spectra. The H α and H β line profiles calculated in NLTE and LTE with our final atmospheric parameters

are presented in Fig. A1. For HE2139–5432 and HE0057–5959, the observed spectra are plotted with continuum normalization as provided by David Yong (private communication).

5.3 Surface gravities based on *Gaia* DR2 trigonometric parallaxes

For each star of our sample, *Gaia* DR2 parallaxes (Gaia Collaboration et al. 2018) are available. To calculate distance based surface gravities, we adopted a relation between log *g*, stellar mass, visual magnitude, and bolometric correction. For dwarfs and giants, a mass of 0.7 and 0.8 solar masses was adopted, respectively. Bolometric corrections were adopted from Casagrande & VandenBerg (2014).

For the vast majority of stars in the second *Gaia* data release, reliable distances cannot be obtained by inverting the parallax. A correct inference procedure must instead be used to account for the non-linearity of the transformation and the asymmetry of the resulting probability distribution (Bailer-Jones et al. 2018). For our sample stars, we adopted distances from Bailer-Jones et al. (2018) available at http://www.mpia.de/~calj/gdr2_distances/main.html. Uncertainties in $\log g_{DR2}$ were calculated using the lower and upper bounds on the confidence interval of the distances recommended by Bailer-Jones et al. (2018). For the sample stars at distances closer than $\simeq 1$ kpc and more distant stars, the uncertainties in distances result in log g uncertainties of smaller than 0.08 and 0.20 dex, respectively. An exception is J2209-0028 at $d=2466\pm766$ with log g error of 0.33 dex. It is also worth noting that the Gaia DR2 parallaxes suffer from a systematic shift, which does not exceed 0.1 mas in absolute value (Arenou et al. 2018; Lindegren et al. 2018; Graczyk et al. 2019: Schönrich, McMillan & Ever 2019). Bailer-Jones et al. (2018) calculated distances applying a systematic shift of 0.029 as recommended by Lindegren et al. (2018).

Fig. 3 presents a comparison of distance based surface gravities with our final results and the data from the literature. For the majority of stars, we found our surface gravities to be consistent within the error bars with those, based on distances. Exceptions are HE2139-5432 and J1313-0019. For HE2139-5432, $\log g_{DR2} = 1.71 \pm 0.44$, while we adopted $\log g = 3.0$. HE2139-5432 is a component of a binary system (Arentsen et al. 2018), and its distance based $\log g$ can be underestimated. For J1313-0019, $\log g_{DR2} = 3.85 \pm 0.23$, while we adopted $\log g = 3.0$. Neither analysis of the position of this star on the H-R diagram nor analysis of the Balmer line wings do support high $\log g_{DR2}$. We calculated the NLTE profiles of H α and H β with the model atmosphere 5600/3.5/-4 (Fig. 2) and obtained that their wings are too strong compared with the observed spectra, while the theoretical profiles in the 5400/3.0/-4 (our final $T_{\text{eff}}/\log g$) model match the observations well.

We note that, for J1029+1729, Caffau et al. (2012) adopted $T_{\rm eff}/\log g = 5811$ K/4.0 despite the fact that the Ca I/Ca II ionization equilibrium was achieved in NLTE with log g = 4.8. Based on the *Gaia* DR2, Bonifacio et al. (2018) came to the conclusion that this star is, indeed, a dwarf. This is fully consistent with our determination.

5.4 Calcium and magnesium abundances of the stellar sample

Impact of NLTE on abundance determination: For different stars of the sample, from 2 to 10 lines of calcium and from 1 to 6 lines of magnesium were used for abundance determination. For weak lines of the minority species, such as Ca I and Mg I, NLTE results in weaker lines and larger abundance compared to LTE ($\Delta_{\rm NLTE}$

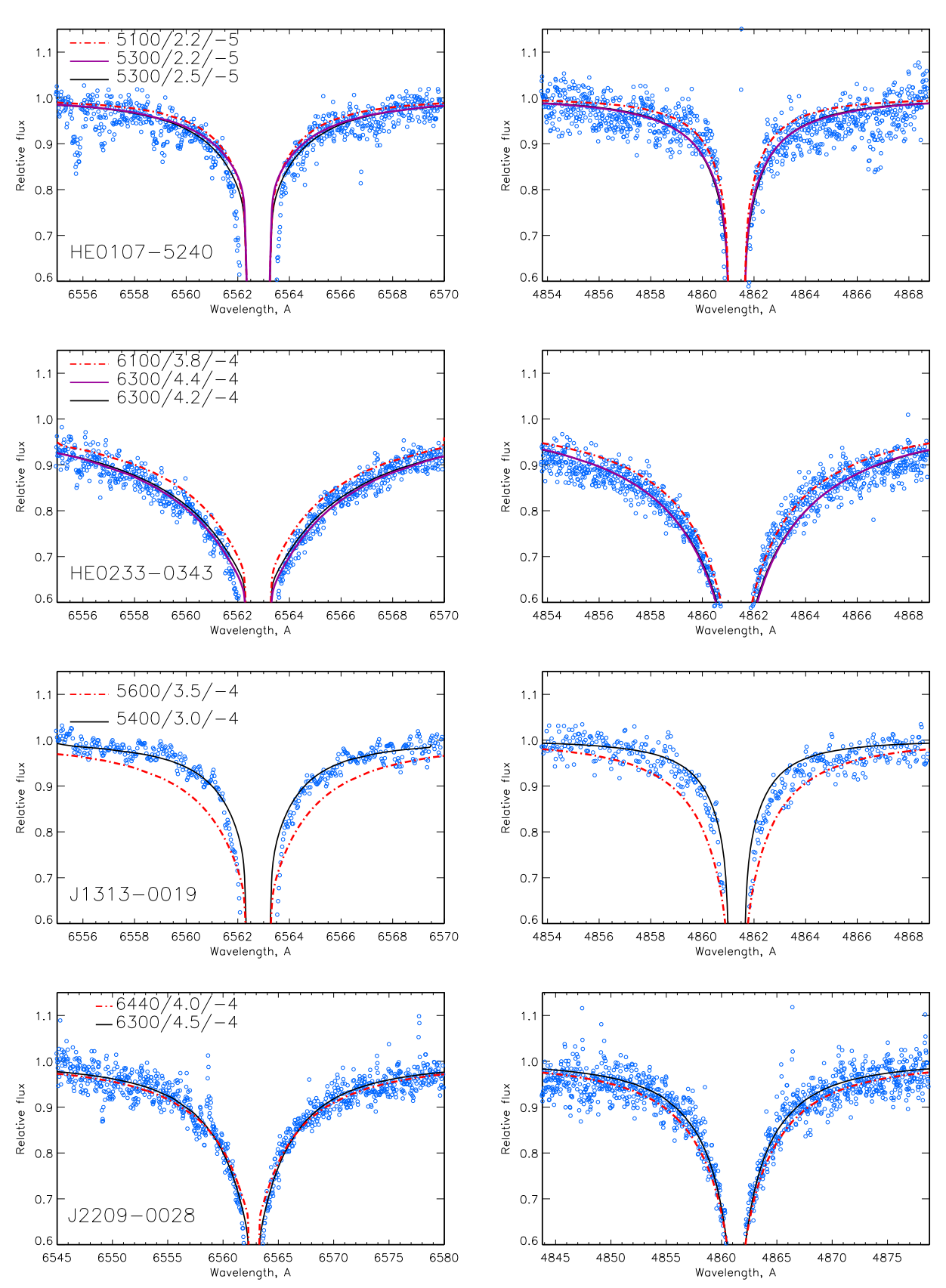


Figure 2. H α (left-hand panels) and H β (right-hand panels) NLTE line profiles calculated with model atmospheres with different parameters for HE0107-5240, HE0233-0343, J1313-0019, and J2209-0028 (from top to bottom).

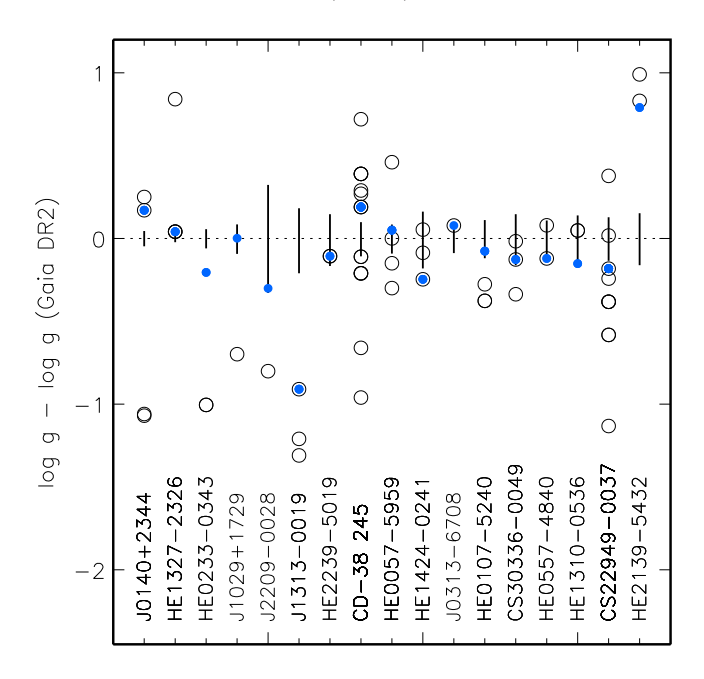


Figure 3. The difference between our final surface gravities and $\log g_{\text{DR2}}$ is shown by filled circles. For comparison, we show the differences between the literature values (multiple determinations) and $\log g_{\text{DR2}}$ by open circles. The uncertainties in $\log g_{\text{DR2}}$ are indicated with dashes. The stars are placed in the order of increasing their distance from the Sun (from left to right).

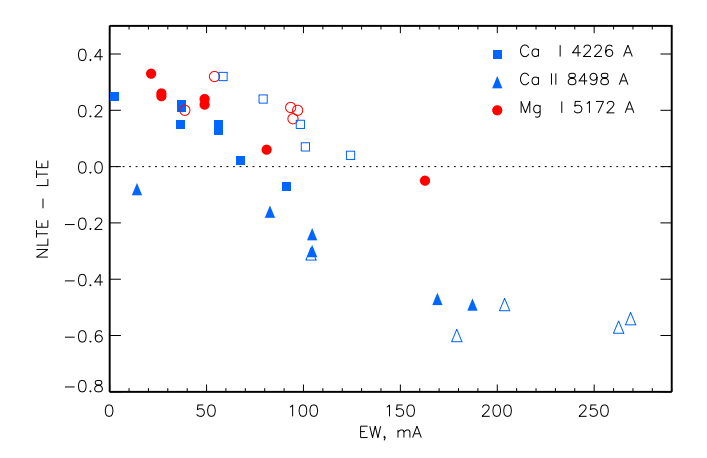


Figure 4. The NLTE abundance corrections for lines of Mg I, Ca I, and Ca II in the sample stars as a function of the line equivalent width. Dwarfs and giants are shown by filled and open symbols, respectively.

> 0) due to an overionisation mechanism caused by superthermal radiation of non-local origin below the thresholds of the Ca I and Mg I low-excitation levels. For strong lines of Ca I and Mg I, with equivalent widths of larger than 60 mÅ, NLTE leads to weaker line wings, but stronger line core, which finally can result in larger total absorbed energy in NLTE compared to LTE and negative NLTE abundance correction ($\Delta_{\rm NLTE} < 0$). A line core strengthens if an upper level of the corresponding transition is depopulated relative to its LTE population in the larger extent compared with the lower level. This happens in the upper atmospheric layers due to photon loss in the investigated line itself. In the metallicity range with what we deal in this study, only the Ca I 4226 Å and Mg I b lines can be strong enough to reveal this effect. The NLTE abundance corrections for Ca I 4226 Å and Mg I 5172 Å vary from -0.1 to 0.3 dex in different stars of our sample (Fig. 4).

Ca II dominates the element number density. No process seems to affect the Ca II ground state population and it keeps its thermodynamic-equilibrium (TE) value. For the excited levels of Ca II, deviations from LTE are ruled by radiative bound-bound transitions. Ca II resonance-line pumping produces a slightly enhanced excitation of the level 4p in the atmospheric layers between $\log \tau_{5000} \simeq 0$ and -1. In the very metal-poor atmospheres, the metastable level 3d is only weakly coupled to the ground state and follows 4p until photon losses in the Ca II IR lines start to depopulate 4p. Overpopulation of 3d level and photon losses in the cores of the Ca II IR triplet lines lead to their strengthening and negative Δ_{NITE} , increasing in absolute value with the equivalent width. For example, from -0.1 to -0.6 dex for the 8498 Å line (Fig. 4). Generally, for the Ca II resonance lines, deviations from LTE are small and lead to a strengthened line core and negative NLTE abundance corrections of not exceeding several hundredth. The smallest NLTE abundance correction of -0.12 dex we found in HE1327–2326 with [Ca/H] = -5.2. In contrast to other stars of the sample, the most metal-poor star known to date, J0313-6708, shows a positive Δ_{NLTE} of 0.14 and 0.23 dex for the Ca II H and K lines, respectively. This happens because these lines wholly form in the layers where Ca II resonance-line pumping overpopulates 4p level relative to its TE population and the line source function exceeds the Planck function.

A problem of underestimated abundance from Ca I 4226 Å and Mg I b lines. In line with the earlier studies of calcium lines in VMP stars by Mashonkina et al. (2007b) and Spite et al. (2012), we found systematically smaller abundance from the Ca_I 4226 Å line compared to those derived from other lines of Ca I and Ca II either in NLTE or in LTE. For stars with $T_{\rm eff} > 5600$ K, the difference between abundance from Ca I 4226 Å and average abundance from the other lines, $\Delta_{4226\text{-Ca}}$, is within 0.1 dex in absolute value and never exceeds the error bars. For cool giants with strong Ca I 4226 Å line, with an equivalent width EW > 60 mÅ, Δ_{4226-C_3} reaches -0.9 dex in LTE, and varies from -0.2 to -0.5 dex in NLTE (Fig. 5). This effect is attended by weakened wings and strengthened core in NLTE, which results in negative NLTE abundance corrections, in contrast to other lines of Ca I and Ca I 4226 Å with EW < 60 mÅ. The NLTE mechanism of the line core strengthening is caused by decrease of the line source function below the Planck function as described by Mashonkina et al. (2007b). Classical 1D model structures with NLTE line formation fail to achieve consistent abundances from Ca I 4226 Å and other calcium lines. Spite et al. (2012) concluded that a fully consistent 3D NLTE line formation modelling is required to shed light on this problem. Full 3D-NLTE calculations for calcium in the most metal-poor star known to date, J0313-6708, were performed by Nordlander et al. (2017). However, only lines of Ca II were detected in the observed spectrum of J0313-6708. For lines of neutral species, 3D leads to strengthened lines and negative abundance corrections (Collet, Asplund & Trampedach 2007; Dobrovolskas et al. 2013), and accounting for this effect by a simple addition of Δ_{3D} and Δ_{NLTE} corrections even increases the discrepancy between the Ca_I 4226 Å line and the other calcium

Using *Hubble Space Telescope* high-resolution spectra around Mg II 2800 Å line, Dupree, Li & Smith (2007) found that metalpoor giants possess chromospheric activity despite of their old age. A semi-empirical model structure, which includes a chromosphere, was constructed by Dupree, Avrett & Kurucz (2016) for the metalpoor giant in ω Cen with $T_{\rm eff}/\log g/[{\rm Fe/H}] = 4745~{\rm K}/1.74/-1.7$. They found the semi-empirical model to be hotter up to 300 K in line-formation layers with respect to classical model structure with

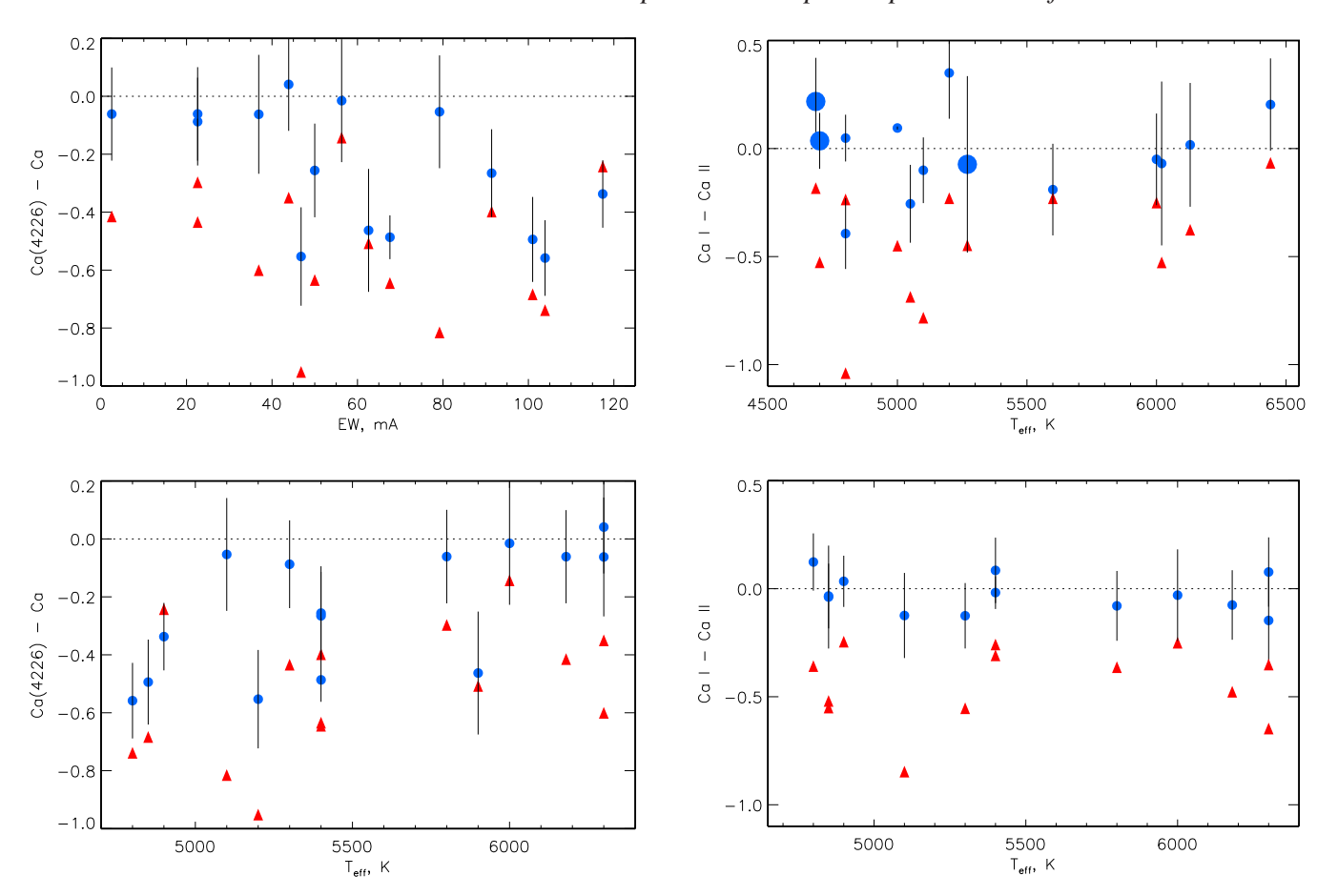


Figure 5. Top panel: Differences between abundances from Ca₁ 4226 Å line and other lines in NLTE (circles) and LTE (triangles) in the sample stars are plotted versus the line equivalent width. Bottom panel: the same values are plotted versus effective temperature. Error bars are shown only for the NLTE case. In LTE, error bars are larger compared to those in NLTE.

the same parameters calculated with ATLAS09 code (Castelli & Kurucz 2004). An increase of temperature in upper atmospheric layers would lead to a weakened core for strong lines of neutral species and higher abundance, while weak lines of neutral species, which form in deep atmospheric layers, and lines of the dominant species will not change.

A similar core-wing effect was described by Mashonkina (2013) for strong Mg Ib lines in the VMP stars. We also obtained negative NLTE abundance corrections for the Mg Ib lines in our two Mgenhanced giants, that is $\Delta_{\rm NLTE}=-0.05$ and -0.07 dex for Mg I 5172 and 5183 Å in HE2139–5432 and $\Delta_{\rm NLTE}=-0.03$ dex for both lines in CS22949–037. For HE2139–5432, NLTE leads to consistent within 0.10 dex abundances from five different lines of Mg I. In CS22949–037, the NLTE wing-core effect and negative $\Delta_{\rm NLTE}=-0.04$ dex were found for one more strong line, Mg I 3829 Å. The NLTE abundances from the Mg I 3829 and 5172 Å lines are found to be 0.2 dex lower compared to those from 4167, 4571, and 5528 Å lines.

Some lines of MgI and CaI 4226 Å were excluded from abundance determination if they show a peculiar behaviour and provide substantially underestimated abundance compared to the other lines

Ca VCa II ionization equilibrium: Fig. 6 shows the Ca I—Ca II abundance differences in NLTE and LTE for 11 stars of our sample calculated with atmospheric parameters derived in this study and in

Figure 6. NLTE (circles) and LTE (triangles) Ca I–Ca II abundance differences for the stars of the sample as a function of $T_{\rm eff}$. Top and bottom panels represent results derived with atmospheric parameters derived in this study and in Ezzeddine et al. (2017), respectively. Large circles represent those stars, where $\log g$ was determined from Fe I–Fe II ionization balance in NLTE.

Ezzeddine et al. (2017). LTE leads to negative Ca I–Ca II abundance differences, of down to -1 dex. While, with our set of atmospheric parameters, for each star, NLTE abundance difference Ca I–Ca II does not exceed 0.1 dex in absolute value. With spectroscopic atmospheric parameters from Ezzeddine et al. (2017), we achieve consistent within the error bars NLTE abundances from Ca I and Ca II for eight stars, while Ca I–Ca II > 0.2 dex in absolute value for the other four stars. For three of these four stars, atmospheric parameters of Ezzeddine et al. (2017) rely only on the lines of Fe I and the derived $\log g$ is uncertain, with an error of 0.4 dex. It is worth noting that among the 12 stars, where abundances from Ca I and Ca II are available, only three of them have lines of both Fe I and Fe II.

5.5 Position on the Hertzsprung-Russell diagram

For each star, the derived effective temperature and surface gravity were checked by comparing its position in the $\log g$ – $T_{\rm eff}$ plane with the theoretical isochrones of 12 and 13 Gyr (total metallicity $z=3.6\mathrm{e}-6$ and $[\alpha/\mathrm{Fe}]=0.4$) in the Yi, Demarque & Kim (2004) grid (Fig. 7). The main sequence and turn-off stars of our sample favour an age of 13 Gyr or slightly higher. For those F-G stars, for which the literature determinations based on the isochrones give two possible surface gravities for a given $T_{\rm eff}$, we

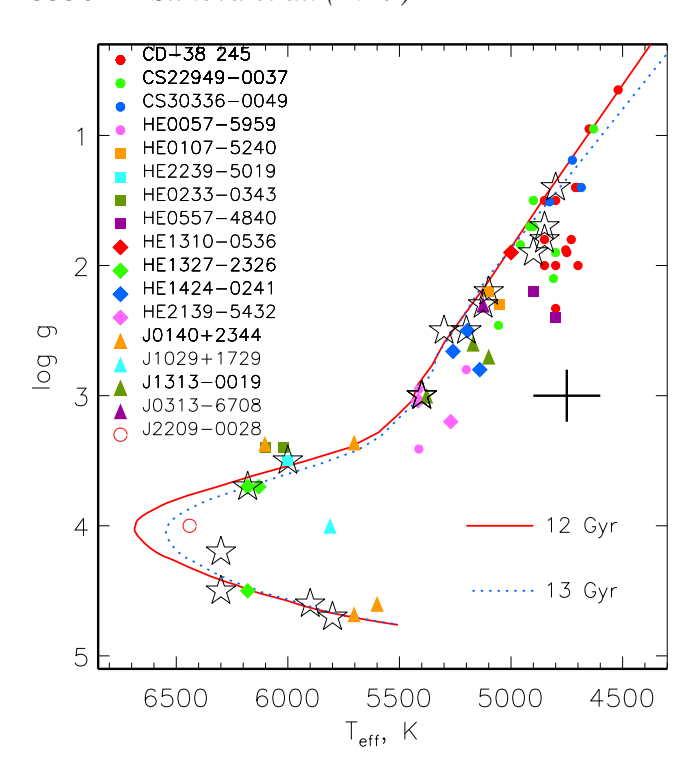


Figure 7. Investigated stars compared with the isochrones of 12 Gyr (solid line) and 13 Gyr (dotted line) for z = 3.5e-6 and $[\alpha/Fe] = 0.4$ from Yi et al. (2004) grid. The large cross indicates $\log g$ and $T_{\rm eff}$ error bars of 0.2 dex and 150 K, respectively. Coloured symbols represent data from the literature, while open stars represent atmospheric parameters adopted in this study.

found an one-valued solution relying on the NLTE analysis of the Ca I/Ca II ionization equilibrium and the *Gaia* DR2 parallax. In line with their old age, our giant stars sit well on the isochrones of 12 and 13 Gyr, which are indistinguishable in the red giant branch. We conclude that HE1327–2326 is a subgiant, in line with Korn et al. (2009), J0140+2344 is a dwarf, in line with Ezzeddine et al. (2017), and J1029+1729 is a dwarf, in line with Bonifacio et al. (2018). For comparison, we also show in Fig. 7 the pairs $T_{\rm eff}$ /log g determined in the literature. For a part of our giant sample, in particular, CD+38 245, CS22939, HE0557–4840, HE1424–0241, HE2139–5432, and J1313–0019, some of the literature effective temperatures are too low to allow the stars to sit on the 12–13 Gyr isochrones. These low temperatures originate from spectroscopic determinations based on the Fe1 excitation equilibrium.

5.6 Notes on individual stars

J0313–6708: For the most iron-deficient star known to date we use three lines of Ca II, namely 3933, 3968, and 8542 Å, to determine abundance, in contrast with the earlier studies by Keller et al. (2014), Bessell et al. (2015), and Nordlander et al. (2017), who relied only on the Ca II H and K lines. Fig. 8 shows the Ca II 8542 Å line in J0313–6708 and the NLTE and LTE profiles calculated with [Ca/H] = -7.09. This line is strong enough (EW = 10 mÅ) to be measured. We found consistent within 0.09 dex NLTE abundances from the three lines, while LTE leads to a discrepancy of 0.5 dex between Ca II 8542 Å and Ca II H and K lines.

We note several stars, for which our final atmospheric parameters differ significantly from the literature data.

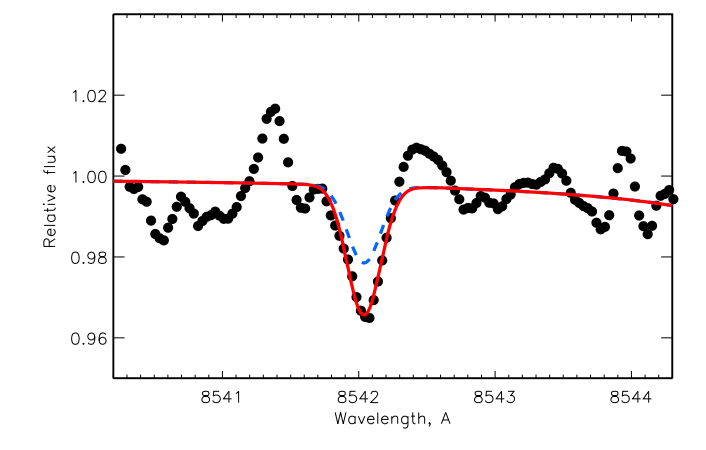


Figure 8. The Ca II 8542 Å line profiles in J0313-6708 calculated with [Ca/H] = -7.09 in NLTE (solid line) and LTE (dashed line). The observed spectrum is shown with circles.

HE0233-0343: We adopted $T_{\rm eff}/\log g=6300/4.20$, while 6100/3.4 and 6020/3.4 were derived by Hansen et al. (2014) and Ezzeddine et al. (2017), respectively. Similarly to HE2239–5019, no line of Fe II was detected in HE0233–0343 and the uncertainty of the Fe I based surface gravity is 0.4 dex. Using 6100 K/3.4 model leads to 0.2 dex difference in NLTE abundance between Ca I and Ca II. The revision is based on photometry and Gaia DR2 parallax. For example, for V-K colour, $T_{\rm eff}=6260$ and 6360 K when using A99 and RM05 calibrations, respectively, and $T_{\rm eff}=6390$ K for V-J colour and RM05 calibration. An extinction E(B-V)=0.024 from Schlegel et al. (1998) was adopted. For HE0233–0343, the Gaia DR2 leads to $\log g=4.44\pm0.06$. An increase of 0.8 dex in $\log g$ compared to the literature data results in an appropriate position on the isochrone and consistent within the error bars abundances from Ca I and Ca II.

HE0107-5240: We adopted $T_{\rm eff}/\log g=5300/2.5$, while the literature data give 5100/2.2 (Christlieb et al. 2004) and 5050/2.2 (Ezzeddine et al. 2017). Photometric effective temperatures calculated with E(B-V)=0.012 are equal to $T_{\rm eff}(V-K)=5300$ K for A99 and RM05 calibrations and $T_{\rm eff}(V-J)=5330$ K for RM05 calibration. With 5100/2.2, we found the NLTE abundance difference, Ca I–Ca II = -0.26 dex, while consistent within 0.1 dex NLTE abundances from Ca I and Ca II are obtained when using 5300 K/2.5.

J1313–0019: We adopted $T_{\rm eff}/\log g=5400/3.3$, while the literature data give 5380/3.0 (Allende Prieto et al. 2015), 5170/2.6 (Frebel et al. 2015), and 5100/2.7 (Ezzeddine et al. 2017). With parameters from Frebel et al. (2015) and Ezzeddine et al. (2017), we found the NLTE abundances from Ca I and Ca II to be consistent within 0.1 dex, while a discrepancy of -0.27 dex is found when using parameters from Allende Prieto et al. (2015). To achieve consistent NLTE abundances from Ca I and Ca II with photometric $T_{\rm eff}=5400$ K, we adopted $\log g=3.3$, which agrees within the error bars with $\log g_{\rm DR2}$. These atmospheric parameters are also supported by the H α and H β line wings (Fig. A1), and the star sits well on the 12–13 Gyr isochrones (Fig. 7).

J2209–0028: We adopted $T_{\rm eff}/\log g = 6300/4.5$, while the literature data give 6440/4.0 (Spite et al. 2013; Ezzeddine et al. 2017). With the adopted stellar parameters we found the NLTE abundances from the Ca I 4226 Å and the Ca II IR triplet lines to be consistent within 0.06 dex, while a discrepancy of 0.18 dex between these lines is found with the literature parameters. For J2209–0028, the

Table 4. The derived NLTE and LTE element abundance ratios.

Star	$T_{\rm eff} \log g \xi_{\rm t}$ (K CGS km s ⁻¹)	[Ca/H]		[Mg/H]		[Ca/Mg]		N_{lines}	
	(K CGS KIIIS)	NLTE	LTE	NLTE	LTE	NLTE	LTE	Ca	Mg
CD-38 245	4850 1.8 2.0	-3.61 ± 0.10	-3.51 ± 1.06	-3.55 ± 0.11	-3.78 ± 0.10	- 0.06	0.27	5	4
CS22949-037	4900 1.9 1.9	-3.35 ± 0.06	-3.45 ± 0.19	-2.52 ± 0.02	-2.67 ± 0.12	-0.83	-0.78	8	3
CS30336-049	4800 1.4 2.1	-3.52 ± 0.07	-3.47 ± 0.27	-3.76 ± 0.09	-3.92 ± 0.08	0.24	0.45	6	4
HE0057-5959	5400 3.0 1.3	-3.17 ± 0.05	-2.97 ± 0.33	-3.30 ± 0.06	-3.35 ± 0.05	0.13	0.38	3	3
HE0107-5240	5300 2.5 1.9	-4.82 ± 0.07	-4.80 ± 0.30	-4.66 ± 0.09	-4.96 ± 0.10	-0.17	0.17	3	2
HE0233-0343	6300 4.2 1.3	-3.72 ± 0.09	-3.32 ± 0.28	-3.64 ± 0.10	-3.86 ± 0.11	-0.08	0.54	4	4
HE0557-4840	5100 2.2 1.9	-4.06 ± 0.04	-3.54 ± 0.44	-3.93 ± 0.05	-4.26 ± 0.09	-0.13	0.73	5	3
HE1310-0536	4850 1.7 2.0	-3.30 ± 0.11	-3.15 ± 0.84	-3.66 ± 0.06	-3.81 ± 0.01	0.36	0.66	3	2
HE1327-2326	6180 3.7 1.7	-5.15 ± 0.06	-5.05 ± 0.16	-3.71 ± 0.00	-4.03 ± 0.01	-1.44	-1.01	5	2
HE1424-0241	5200 2.5 1.8	-4.12 ± 0.08	-3.87 ± 0.22	-3.48 ± 0.01	-3.76 ± 0.09	-0.64	-0.11	4	2
HE2139-5432	5400 3.0 1.3	-3.47 ± 0.05	-3.34 ± 0.42	-2.18 ± 0.05	-2.20 ± 0.11	-1.29	-1.13	5	5
HE2239-5019	6000 3.5 1.4	-3.57 ± 0.02	-3.67 ± 0.18	-3.25 ± 0.06	-3.56 ± 0.09	-0.32	-0.11	2	3
J0140+2344	5900 4.6 0.9	-3.18 ± 0.07	-3.20 ± 0.11	-3.20 ± 0.09	-3.37 ± 0.10	0.02	0.17	2	3
J0313-6708	5125 2.3 2.0	-7.12 ± 0.05	-7.09 ± 0.39	-3.96 ± 0.02	-4.25 ± 0.01	-3.15	-2.84	3	2
J1029+1729	5800 4.7 0.8	-4.48 ± 0.06	-4.35 ± 0.20	-4.38 ± 0.07	-4.51 ± 0.08	-0.10	0.16	4	4
J1313-0019	5400 3.0 1.5	-4.10 ± 0.06	-3.80 ± 0.23	-4.10 ± 0.08	-4.21 ± 0.04	0.00	0.41	3	2
J2209-0028	6300 4.5 1.2	-3.68 ± 0.04	-3.45 ± 0.21	-3.85 ± 0.14	-4.09 ± 0.15	0.17	0.64	4	3
Atmospheric para	meters from Ezzeddine	et al. (2017):							
CD-38 245	4700 2.0 2.2	-3.74 ± 0.07	-3.61 ± 0.76	-3.85 ± 0.31	-3.90 ± 0.13	0.11	0.29	5	4
CS22949-037	4800 1.9 1.9	-3.44 ± 0.07	-3.54 ± 0.18	-2.60 ± 0.06	-2.75 ± 0.16	-0.84	-0.79	8	3
CS30336-049	4685 1.4 2.1	-3.62 ± 0.18	-3.70 ± 0.11	-3.91 ± 0.11	-4.01 ± 0.11	0.29	0.30	6	4
HE0057-5959	5200 2.8 1.9	-3.35 ± 0.26	-3.18 ± 0.17	-3.48 ± 0.06	-3.62 ± 0.09	0.13	0.44	2	3
HE0107-5240	5050 2.3 2.2	-5.04 ± 0.16	-4.96 ± 0.50	-5.27 ± 0.04	-5.54 ± 0.06	0.23	0.58	3	2
HE0233-0343	6020 3.4 2.0	-4.06 ± 0.12	-3.84 ± 0.25	-3.79 ± 0.08	-4.06 ± 0.08	-0.27	0.22	3	4
HE0557-4840	4800 2.4 1.8	-4.11 ± 0.05	-3.53 ± 0.01	-4.32 ± 0.06	-4.50 ± 0.05	0.21	0.97	3	3
HE1310-0536	5000 1.9 2.2	-3.27 ± 0.05	-3.11 ± 0.69	-3.58 ± 0.06	-3.75 ± 0.01	0.31	0.64	3	2
HE1327-2326	6130 3.7 2.1	-5.19 ± 0.15	-5.11 ± 0.22	-3.70 ± 0.01	-4.03 ± 0.01	-1.49	-1.08	5	2
HE1424-0241	5140 2.8 2.2	-4.18 ± 0.07	-3.92 ± 0.20	-3.68 ± 0.03	-3.82 ± 0.02	-0.50	-0.09	3	2
HE2139-5432	5270 3.2 1.0	-3.52 ± 0.22	-3.36 ± 0.79	-2.37 ± 0.24	-2.40 ± 0.18	-1.15	-0.96	4	5
HE2239-5019	6000 3.5 1.8	-3.63 ± 0.04	-3.72 ± 0.18	-3.31 ± 0.02	-3.61 ± 0.05	-0.33	-0.11	23	3
J0140+2344	5600 4.6 1.0	-3.75 ± 0.15	-3.75 ± 0.15	-3.51 ± 0.06	-3.63 ± 0.07	-0.24	-0.12	1	3
J1029+1729	5811 4.0 1.5	-4.66 ± 0.12	-4.56 ± 0.11	-4.34 ± 0.11	-4.55 ± 0.13	-0.32	-0.01	4	4
J1313-0019	5100 2.7 1.8	-4.47 ± 0.01	-4.12 ± 0.29	-4.32 ± 0.01	-4.52 ± 0.04	-0.15	0.40	3	2
J2209-0028	6440 4.0 1.3	-3.68 ± 0.16	-3.63 ± 0.13	-3.77 ± 0.08	-4.00 ± 0.08	0.09	0.38	5	3

Gaia DR2 leads to $\log g = 4.80 \pm 0.33$. The J,H, and K magnitudes are not available, and $T_{\rm eff}$ (V-I) = 6280 and 6550 K when using RM05 and A99 calibrations, respectively, and E(B-V) = 0.08. The adopted atmospheric parameters are supported by the $H\alpha$ and $H\beta$ line wings (Fig. 2), and the star sits well on the 12–13 Gyr isochrones (Fig. 7).

6 CALCIUM TO MAGNESIUM ABUNDANCE RATIOS

Table 4 presents [Ca/Mg] NLTE and LTE abundance ratios, derived with atmospheric parameters from this study and from Ezzeddine et al. (2017). For different stars, in NLTE, our [Ca/H] ratios vary from -7.1 to -3.2, while [Mg/H] spans the -4.7 to -2.2 range. Fig. 9 shows [Ca/Mg] NLTE and LTE abundance ratios derived with our final atmospheric parameters. We divided our sample stars into five groups depending on the derived [Ca/Mg] ratio.

For 10 stars, we found close to solar [Ca/Mg] NLTE abundance ratios, while in LTE, [Ca/Mg] shows a large spread and varies from -0.1 to 0.7.

For the two stars, namely CS30336-049 and HE1310-0536, we found positive [Ca/Mg] NLTE ratios of 0.24 and 0.36, respectively.

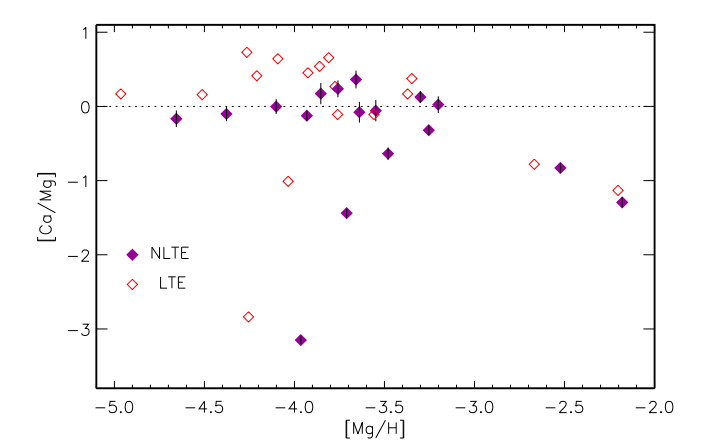
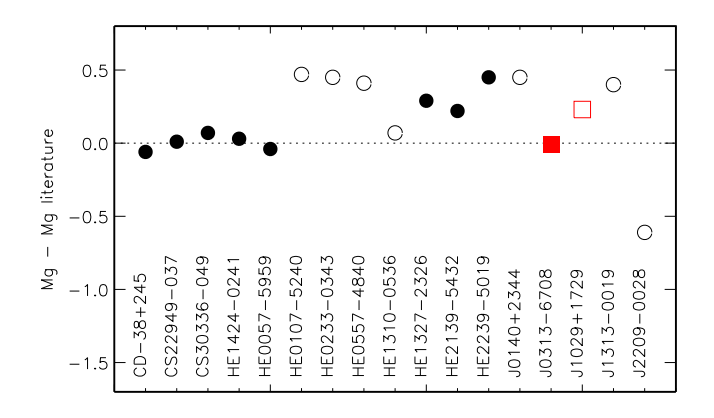


Figure 9. [Ca/Mg] NLTE (filled symbols) and LTE (open symbols) abundance ratios for the sample stars.

HE1424-0241 is a Ca-deficient star as found by Cohen et al. (2007) and we obtain low [Ca/Mg] = -0.83. This is a rare type of stars and it comprises 10 per cent of stars with [Fe/H] < -3 that do not reveal carbon enhancement (Cohen et al. 2013).



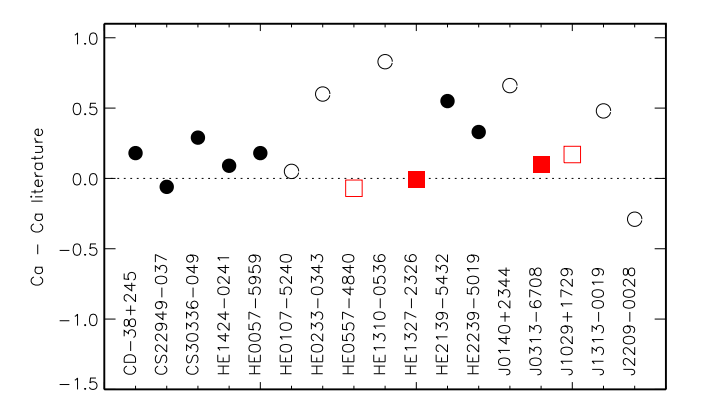


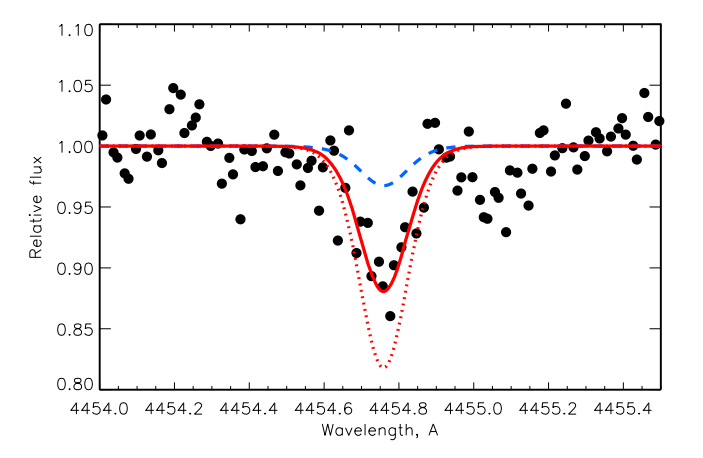
Figure 10. Comparison of magnesium and calcium NLTE abundances derived with atmospheric parameters adopted in this study with the data from the literature. Abundance differences in stars, where adopted $T_{\rm eff}$ and $\log g$ differ from those in the literature are shown with open symbols. Stars, where NLTE and LTE literature abundances are available, are shown with squares and circles, respectively.

For the three stars, namely CS22949-037, HE2139-5432, and HE1327-2326, we derived very low [Ca/Mg] ratio of -0.83, -1.29, and -1.44, respectively. In contrast to the Ca-deficient stars, this is a result of magnesium enhancement, with [Mg/H] = -2.52, -2.18, and -3.71, respectively, according to our determinations. These stars are known to be rich also in carbon, nitrogen, and oxygen, as found by Depagne et al. (2002), Cayrel et al. (2004), Aoki et al. (2006), Frebel et al. (2008), and Yong et al. (2013). Element abundance pattern of these stars can be explained by nucleosynthesis in a faint SN (Nomoto 2012).

For the most iron-poor star known to date, J0313-6708, we found an extreme value of [Ca/Mg] = -3.15 in line with Keller et al. (2014).

When using atmospheric parameters from Ezzeddine et al. (2017), we obtain [Ca/Mg] abundance ratios in individual stars to be similar to those determined with our final atmospheric parameters, although the errors in abundance increases together with a scatter in [Ca/Mg] for those 10 stars with solar ratios.

We compared our NLTE magnesium and calcium abundances with the earlier determinations from the literature (Fig. 10). For J0313-6708 and J1029+1729, NLTE abundances of magnesium and calcium were determined by Nordlander et al. (2017, NLTE, 1D) and Caffau et al. (2012), respectively. For HE0557-4840 and HE1327-2326, calcium NLTE abundances were determined by Norris et al. (2007) and Korn et al. (2009), respectively. For



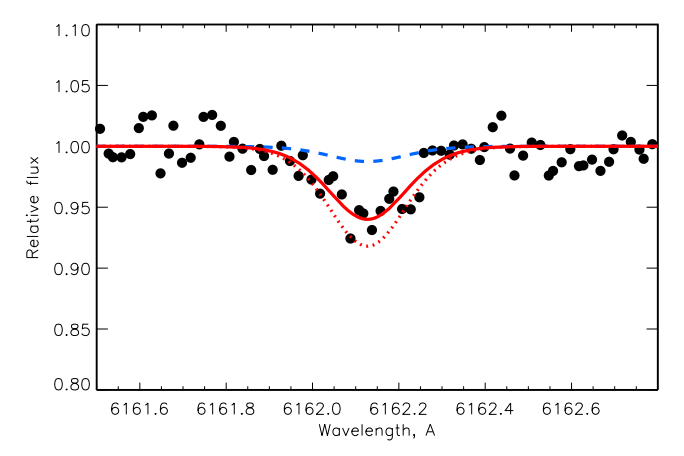


Figure 11. Ca1 4454 Å (top panel) and 6172 Å (bottom panel) lines in observed spectrum of HE1310–0536 (circles). The line profiles are calculated with [Ca/H] = -3.27 in NLTE (solid line) and LTE (dotted line) and with [Ca/H] = -4.15 in LTE (dashed line) as determined by Hansen et al. (2015).

HE1327–2326 and J0313–6708, where our adopted $T_{\rm eff}$ and $\log g$ agree with the literature data, our NLTE abundances are consistent with the earlier NLTE determinations. For the other stars, only LTE abundance determinations are available in the literature. Our magnesium and calcium NLTE abundances are prevalently larger compared to those LTE. Positive abundance differences can be explained with the NLTE effects. For lines of Mg I and Ca I, NLTE results in up to 0.4 dex higher abundance compared to LTE. The largest discrepancy of 0.9 dex we found for calcium abundance in HE1310-0536, investigated by Hansen et al. (2015). This discrepancy cannot be explained with the NLTE effects only. Using atmospheric parameters from Hansen et al. (2015), we calculated NLTE and LTE profiles of the Ca_I 4454 and 6162 Å lines in HE1310-0536. Fig. 11 shows our best NLTE fits together with LTE synthetic spectra and LTE synthetic spectra, calculated with calcium abundance from Hansen et al. (2015). We cannot fit Ca I 4454 and 6162 Å in HE1310-0536 with atmospheric parameters and abundance [Ca/H] = -4.15 from Hansen et al. (2015) either in LTE, or in NLTE.

7 CONCLUSIONS

The most metal-poor stars are the oldest objects, they provide a unique opportunity to study the earliest epoch of the Galaxy formation and individual nucleosynthesis events. These stars should be investigated with a scrupulous care, taking into account all available photometric, spectroscopic, and astrometric information.

We determined atmospheric parameters for 17 ultra metal-poor stars, using an extensive method based on careful inspection of photometric colour– $T_{\rm eff}$ calibrations, *Gaia* DR2 trigonometric parallaxes, inspecting the star position on the 12 and 13 Gyr isochrones, and NLTE analysis of the Ca I/Ca II ionization equilibrium and the Balmer line wings.

The following observational data are still required to constrain better atmospheric parameters of the sample stars:

- (i) HE2239-5019 and J0140+2344: spectra covering the Ca II IR triplet;
- (ii) J2209-0028: accurate JHK magnitudes, spectra covering the Mg Ib lines;
- (iii) HE0057-5959, HE2139-5432, and HE2239-5019: accurate visible and IR photometry.

Model atom of Ca I II from Mashonkina et al. (2017) was updated by including quantum-mechanical rate coefficients for the Ca I + H I and Ca II + H I collisions from Belyaev et al. (2017) and Belyaev et al. (2018), respectively. For different lines of Ca I in our sample stars, the abundance difference between employing rate coefficients from Belyaev et al. (2017) and Mitrushchenkov et al. (2017) does not exceed 0.05 dex. The same is true for lines of Ca II and the abundance difference between employing accurate data of Belyaev et al. (2018) and classical Drawinian rates for the Ca II + H I collisions.

We determined magnesium and calcium NLTE and LTE abundances of our sample stars. For each star, abundances from different lines of Ca I and Ca II are found to be consistent. An exception is the Ca I 4226 Å line. If this line is strong, with an equivalent width of larger than about 50 mÅ, it gives up to 0.8 dex lower abundance compared to that from the other lines, independent of NLTE or LTE. If this line is weaker, it provides the NLTE abundance, which is consistent with that from the other lines, and Ca I 4226 Å can be used for abundance determination. Application of accurate quantum-mechanical data for Ca I + H I collisions does not help to make a progress in the solution of this long-standing problem (Mashonkina et al. 2007b; Spite et al. 2012; Mashonkina et al. 2017).

For 10 stars, we found close-to-solar [Ca/Mg] NLTE abundance ratios. In the remaining stars, magnesium and calcium abundances do not follow each other, such that [Ca/Mg] varies between -3.15 and +0.36, arguing for a small number of nucleosynthesis events contributed to their chemical abundances.

The obtained atmospheric parameters will be used in the forthcoming paper to determine NLTE abundances of chemical elements observed in spectra of the UMP stars.

ACKNOWLEDGEMENTS

This study is based on spectral observations retrieved from the ESO Science Archive Facility; the Keck Observatory Archive (KOA), which is operated by the W. M. Keck Observatory and the NASA Exoplanet Science Institute (NExScI), under contract with the National Aeronautics and Space Administration. We thank David Yong and John Norris for providing stellar spectra for CS30336–049, HE0057–5959, HE2139–5432, and J140+2344. We made use of the SIMBAD data base, operated at CDS, Strasbourg, France; NASA/IPAC Infrared Science Archive, which is operated by the Jet Propulsion Laboratory, California Institute of Technology, under contract with the National Aeronautics and Space Administration; MARCS; and VALD data bases. This work has made use of data

from the European Space Agency (ESA) mission *Gaia* (https://www.cosmos.esa.int/gaia), processed by the *Gaia* Data Processing and Analysis Consortium (DPAC, https://www.cosmos.esa.int/web/gaia/dpac/consortium). Funding for the DPAC has been provided by national institutions, in particular the institutions participating in the *Gaia* Multilateral Agreement. TS acknowledges financial support from the Presidium RAS Programme P-12 ÀProblems of Origin and Evolution of the Universe'. LM acknowledges financial support from the Russian Scientific Foundation (grant no. 17-13-01144). RE acknowledges support from JINA-CEE, funded in part by the National Science Foundation under grant no. PHY-1430152. We thank the referee for comments and suggestions.

REFERENCES

Ahn C. P. et al., 2012, ApJS, 203, 21

Allende Prieto C. et al., 2015, A&A, 579, A98

Alonso A., Arribas S., Martinez-Roger C., 1996, A&A, 313, 873 (A99)

Alonso A., Arribas S., Martínez-Roger C., 1999, A&AS, 140, 261

Amarsi A. M., Lind K., Asplund M., Barklem P. S., Collet R., 2016, MNRAS, 463, 1518

Amarsi A. M., Nordlander T., Barklem P. S., Asplund M., Collet R., Lind K., 2018, A&A, 615, A139

Andrievsky S. M., Spite M., Korotin S. A., Spite F., Bonifacio P., Cayrel R., François P., Hill V., 2010, A&A, 509, A88

Aoki W., Frebel A., Christlieb N., Norris J. E., Beers T. C., Minezaki T., Barklem P. S., Honda S., 2006, ApJ, 639, 897

Aoki W. et al., 2013, AJ, 145, 13

Arenou F., Luri X., Babusiaux C., Fabricius C., Helmi A., Muraveva T., Robin A. C., Spoto F., 2018, A&A, 616, A17

Arentsen A., Starkenburg E., Shetrone M. D., Venn K. A., Depagne É., McConnachie A. W., 2019, A&A, 621, A108

Bailer-Jones C. A. L., Rybizki J., Fouesneau M., Mantelet G., Andrae R., 2018, AJ, 156, 58

Barklem P. S., Belyaev A. K., Spielfiedel A., Guitou M., Feautrier N., 2012, A&A, 541, A80

Barklem P. S., Piskunov N., O'Mara B. J., 2000, A&A, 363, 1091

Beers T., Christlieb N., 2005, ARA&A, 43, 531

Beers T. C. et al., 2007, ApJS, 168, 128

Belyaev A. K., Voronov Y. V., Gadéa F. X., 2018, ApJ, 867, 87

Belyaev A. K., Voronov Y. V., Yakovleva S. A., Mitrushchenkov A., Guitou M., Feautrier N., 2017, ApJ, 851, 59

Bergemann M., Lind K., Collet R., Magic Z., Asplund M., 2012, MNRAS, 427, 27

Bernstein R., Shectman S. A., Gunnels S. M., Mochnacki S., Athey A. E., 2003, in Iye M., Moorwood A. F. M., eds, Proc. SPIE Conf. Ser. Vol. 4841, Instrument Design and Performance for Optical/Infrared Groundbased Telescopes. SPIE, Bellingham, p. 1694

Bessell M. S., Christlieb N., Gustafsson B., 2004, ApJ, 612, L61

Bessell M. S. et al., 2015, ApJ, 806, L16

Bonifacio P., Caffau E., Spite M., Spite F., Francois P., Zaggia S., Arenou F., Haigron R., 2018, Research Notes of the American Astronomical Society, 2, 19

Butler K., Giddings J., 1985, Newsletter on the Analysis of Astronomical Spectra, No. 9. Department of Physics and Astronomy, University College of London

Caffau E. et al., 2011, Nature, 477, 67

Caffau E. et al., 2012, A&A, 542, A51

Casagrande L., VandenBerg D. A., 2014, MNRAS, 444, 392

Castelli F., Kurucz R. L., 2004, preprint (arXiv:astro-ph/0405087)

Cayrel R. et al., 2004, A&A, 416, 1117

Christlieb N., Gustafsson B., Korn A. J., Barklem P. S., Beers T. C., Bessell M. S., Karlsson T., Mizuno-Wiedner M., 2004, ApJ, 603, 708

Cohen J. G., Christlieb N., Thompson I., McWilliam A., Shectman S., Reimers D., Wisotzki L., Kirby E., 2013, ApJ, 778, 56 Cohen J. G., McWilliam A., Christlieb N., Shectman S., Thompson I., Melendez J., Wisotzki L., Reimers D., 2007, ApJ, 659, L161

Collet R., Asplund M., Trampedach R., 2007, A&A, 469, 687

Depagne E. et al., 2002, A&A, 390, 187

Dobrovolskas V., Kučinskas A., Steffen M., Ludwig H.-G., Prakapavičius D., Klevas J., Caffau E., Bonifacio P., 2013, A&A, 559, A102

Drawin H.-W., 1968, Z. Phys., 211, 404

Drawin H.-W., 1969, Z. Phys., 225, 483

Dupree A. K., Avrett E. H., Kurucz R. L., 2016, ApJ, 821, L7

Dupree A. K., Li T. Q., Smith G. H., 2007, AJ, 134, 1348

Ezzeddine R., Frebel A., 2018, ApJ, 863, 168

Ezzeddine R., Frebel A., Plez B., 2017, ApJ, 847, 142

Frebel A., Aoki W., Christlieb N., Ando H., Asplund M., Barklem P. S., Beers T., Eriksson K., 2005, Nature, 434, 871

Frebel A., Casey A. R., Jacobson H. R., Yu Q., 2013, ApJ, 769, 57

Frebel A., Chiti A., Ji A. P., Jacobson H. R., Placco V. M., 2015, ApJ, 810, L27

Frebel A., Christlieb N., Norris J. E., Aoki W., Asplund M., 2006, ApJ, 638, L17

Frebel A., Collet R., Eriksson K., Christlieb N., Aoki W., 2008, ApJ, 684, 588

Frebel A., Ji A. P., Ezzeddine R., Hansen T. T., Chiti A., Thompson I. B., Merle T., 2019, ApJ, 871, 146

Fuhrmann K., 1998, A&A, 338, 161

Gaia Collaboration et al., 2018, A&A, 616, A1

Graczyk D., Pietrzyński G., Gieren W., Storm J., Nardetto N., Gallenne A., Maxted P. F. L., Kervella P., 2019, ApJ, 872, 85

Gustafsson B., Edvardsson B., Eriksson K., Jørgensen U. G., Nordlund Å., Plez B., 2008, A&A, 486, 951

Hansen C. J., Bergemann M., Cescutti G., François P., Arcones A., Karakas A. I., Lind K., Chiappini C., 2013, A&A, 551, A57

Hansen T. et al., 2014, ApJ, 787, 162

Hansen T. et al., 2015, ApJ, 807, 173

Heger A., Woosley S. E., 2010, ApJ, 724, 341

Jacobson H. R. et al., 2015, ApJ, 807, 171

Jordi K., Grebel E. K., Ammon K., 2006, A&A, 460, 339

Keller S. C. et al., 2014, Nature, 506, 463

Korn A. J., Richard O., Mashonkina L., Bessell M. S., Frebel A., Aoki W., 2009, ApJ, 698, 410

Kupka F., Piskunov N., Ryabchikova T. A., Stempels H. C., Weiss W. W., 1999, A&AS, 138, 119

Lai D. K., Bolte M., Johnson J. A., Lucatello S., Heger A., Woosley S. E., 2008, ApJ, 681, 1524

Limongi M., Chieffi A., Bonifacio P., 2003, ApJ, 594, L123

Lindegren L. et al., 2018, A&A, 616, A2

Lind K. et al., 2017, MNRAS, 468, 4311

Mashonkina L., Korn A., Przybilla N., 2007a, in Mashonkina L., Sachkov M., eds, Proceedings of the Conference held 13-15 September 2006, Spectroscopic Methods in Modern Astrophysics. Yanus-K, Moscow, Russia, p. 115

Mashonkina L., 2013, A&A, 550, A28

Mashonkina L., Christlieb N., Barklem P. S., Hill V., Beers T. C., Velichko A., 2010, A&A, 516, A46

Mashonkina L., Gehren T., Shi J.-R., Korn A. J., Grupp F., 2011, A&A, 528,

Mashonkina L., Jablonka P., Pakhomov Y., Sitnova T., North P., 2017, A&A, 604, A129

Mashonkina L., Korn A. J., Przybilla N., 2007b, A&A, 461, 261

Mashonkina L., Sitnova T., Belyaev A. K., 2017, A&A, 605, A53

Mashonkina L. et al., 2008, A&A, 478, 529

McWilliam A., Preston G. W., Sneden C., Searle L., 1995, AJ, 109, 2757

Mitrushchenkov A., Guitou M., Belyaev A. K., Yakovleva S. A., Spielfiedel A., Feautrier N., 2017, J. Chem. Phys., 146, 014304

Nomoto K., 2012, in Aoki W., Ishigaki M., Suda T., Tsujimoto T., Arimoto N., eds, ASP Conf. Ser. Vol. 458, Nucleosynthesis in Hypernovae and Faint Supernovae and Abundance Patterns of Extremely Metal-Poor Stars. Astron. Soc. Pac., San Francisco, p. 3

Nordlander T., Amarsi A. M., Lind K., Asplund M., Barklem P. S., Casey A. R., Collet R., Leenaarts J., 2017, A&A, 597, A6

Norris J. E., Ryan S. G., Beers T. C., 2001, ApJ, 561, 1034

Norris J. E., Christlieb N., Bessell M. S., Asplund M., Eriksson K., Korn A. J., 2012, ApJ, 753, 150

Norris J. E., Christlieb N., Korn A. J., Eriksson K., Bessell M. S., Beers T. C., Wisotzki L., Reimers D., 2007, ApJ, 670, 774

Norris J. E. et al., 2013, ApJ, 762, 25

Placco V. M., Frebel A., Lee Y. S., Jacobson H. R., Beers T. C., Pena J. M., Chan C., Heger A., 2015, ApJ, 809, 136

Placco V. M. et al., 2016, ApJ, 833, 21

Ramírez I., Meléndez J., 2005, ApJ, 626, 465 (RM05)

Roederer I. U., Sneden C., Lawler J. E., Sobeck J. S., Cowan J. J., Boesgaard A. M., 2018, ApJ, 860, 125

Roederer I. U., Preston G. W., Thompson I. B., Shectman S. A., Sneden C., Burley G. S., Kelson D. D., 2014, AJ, 147, 136

Roederer I. U. et al., 2012, ApJS, 203, 27

Ryabchikova T., Piskunov N., Kurucz R. L., Stempels H. C., Heiter U., Pakhomov Y., Barklem P. S., 2015, Phys. Scr, 90, 054005

Ryabchikova T. et al., 2016, MNRAS, 456, 1221

Ryan S. G., Norris J. E., Beers T. C., 1996, ApJ, 471, 254

Schlegel D. J., Finkbeiner D. P., Davis M., 1998, ApJ, 500, 525

Schönrich R., McMillan P., Eyer L., 2019, preprint (arXiv:1902.02355)

Seaton M. J., Yan Y., Mihalas D., Pradhan A. K., 1994, MNRAS, 266, 805
Sitnova T., Mashonkina L., Pakhomov Y., 2018, in Recio-Blanco A., de Laverny P., Brown A. G. A., Prusti T., eds, Proc. IAU Symp. 330, Astrometry and Astrophysics in the Gaia Sky, Cambridge University Press p. 327

Skrutskie M. F., Cutri R., Stiening R., Weinberg M. D., Schneider S., Carpenter J. M., Beichman C., Capps R., 2006, AJ, 131, 1163

Spite M., Caffau E., Bonifacio P., Spite F., Ludwig H.-G., Plez B., Christlieb N., 2013, A&A, 552, A107

Spite M. et al., 2012, A&A, 541, A143

Tsymbal V., 1996, in Adelman S. J., Kupka F., Weiss W. W.eds, ASP Conf. Ser. Vol. 108, STARSP: A Software System For the Analysis of the Spectra of Normal Stars. Astron. Soc. Pac., San Francisco, p. 198

Tsymbal V., Ryabchikova T., Sitnova T., 2019, in Romanyuk I. I., Yakunin I. A., Kudryavtsev D. O., eds, Physics of magnetic stars. Astron. Soc. Pas., San Francisco, in press

van Leeuwen F., 2007, A&A, 474, 653

Vidal C. R., Cooper J., Smith E. W., 1970, J. Quant. Spec. Radiat. Transf., 10, 1011

Vidal C. R., Cooper J., Smith E. W., 1973, ApJS, 25, 37

Wenger M. et al., 2000, A&AS, 143, 9

Wu X. S., Alexeeva S., Mashonkina L., Wang L., Zhao G., Grupp F., 2015, A&A, 577, A134

Yi S. K., Demarque P., Kim Y.-C., 2004, Ap&SS, 291, 261

Yong D. et al., 2013, ApJ, 762, 26

Zhao G., Butler K., Gehren T., 1998, A&A, 333, 219

APPENDIX

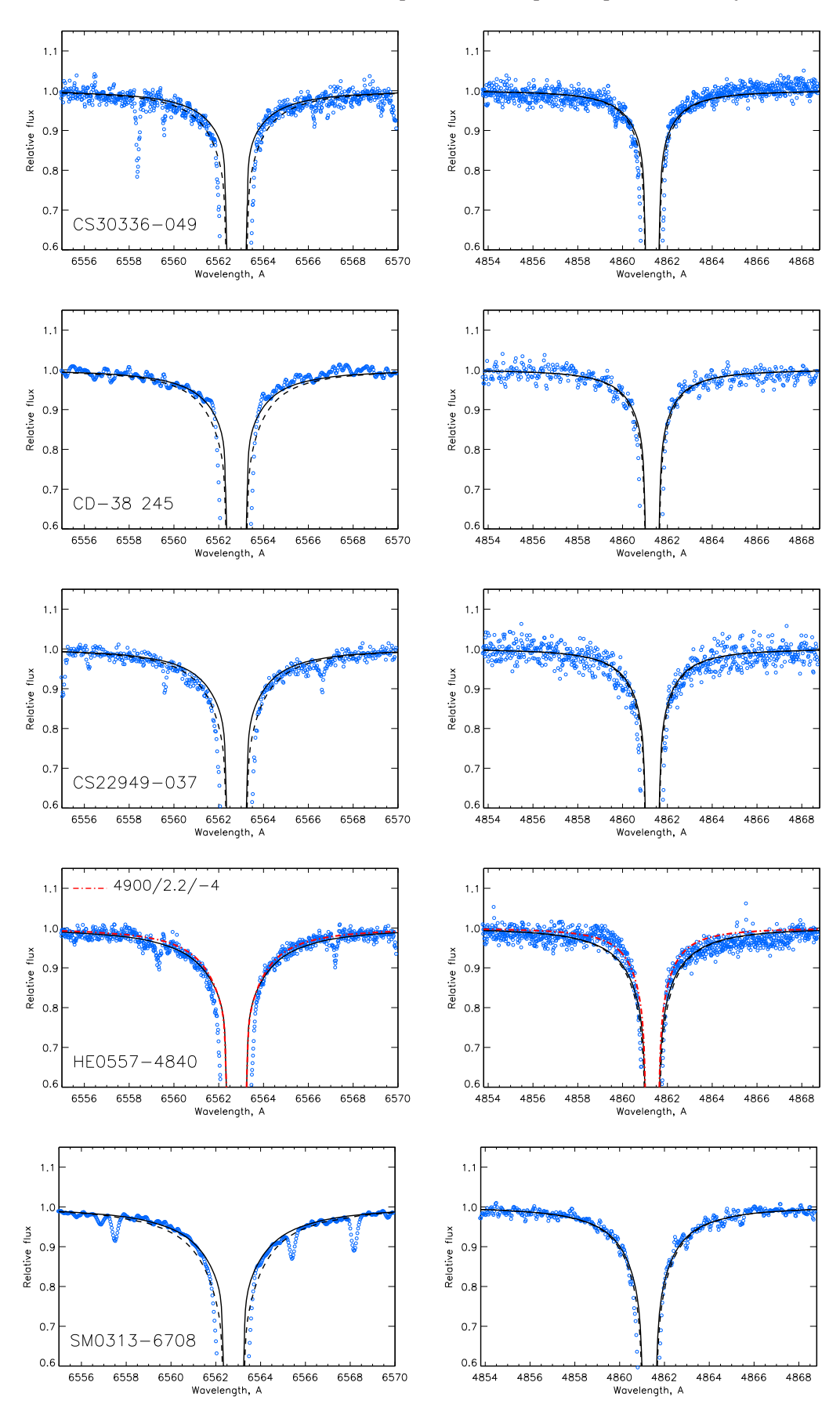


Figure A1. NLTE (solid lines) and LTE (dashed lines) profiles of the H α (left-hand column) and H β (right-hand column) lines in the sample stars.

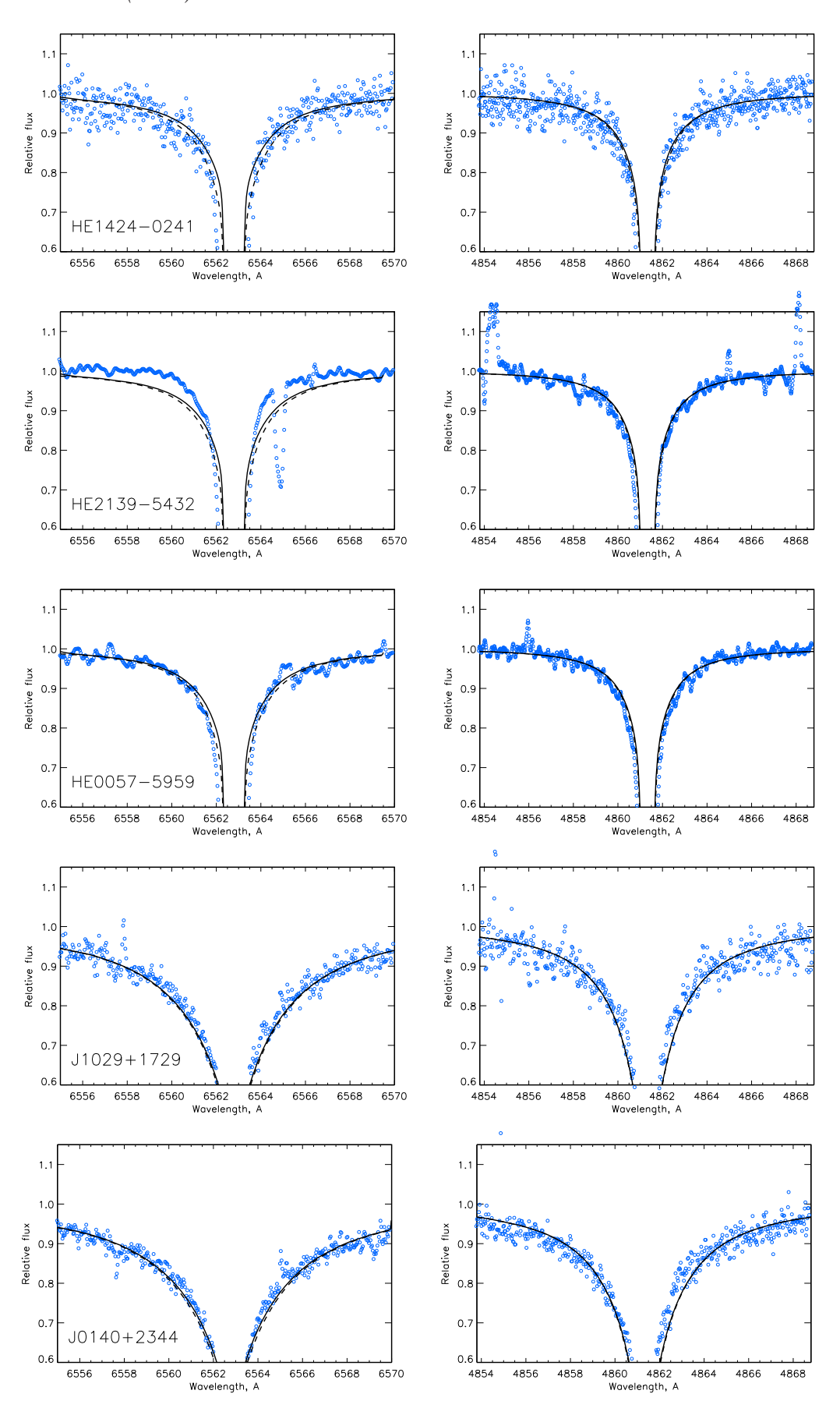


Figure A1 - Continued

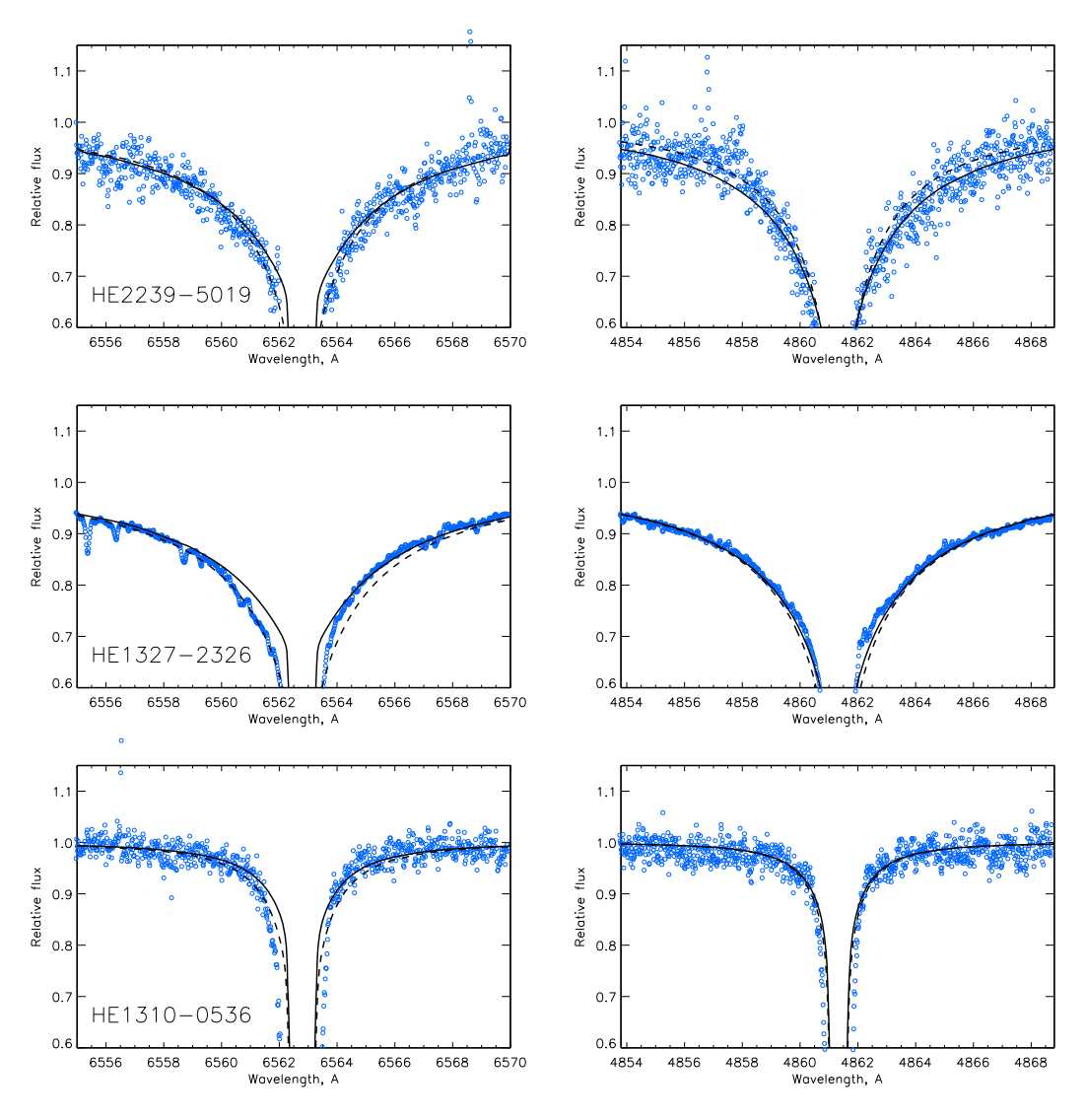


Figure A1 - Continued

This paper has been typeset from a $T_EX/I_E^2T_EX$ file prepared by the author.